THE JOURNAL OF PHYSICAL CHEMISTRY A
A JOURNAL OF THE AMERICAN CHEMICAL SOCIETY

pubs.acs.org/JPCA

Article

Combined Spectroscopic and Computational Investigation on the Oxidation of *exo*-Tetrahydrodicyclopentadiene (JP-10; $C_{10}H_{16}$) Doped with Titanium−Aluminum−Boron Reactive Metal Nanopowder

Stephen J. Brotton, Sahan D. Perera, Anupam Misra, N. Fabian Kleimeier, Andrew M. Turner, Ralf I. Kaiser,* Mark Palenik,* Matthew T. Finn, Albert Epshteyn,* Bing-Jian Sun, Li-Jie Zhang, and Agnes H. H. Chang*

Cite This: *J. Phys. Chem. A* 2022, 126, 125−144

Read Online

ACCESS | Metrics & More | Article Recommendations | Supporting Information

ABSTRACT: We report the results on the combustion of single, levitated droplets of *exo*-tetrahydrodicyclopentadiene (JP-10) doped with titanium−aluminum−boron (Ti−Al−B) reactive metal nanopowders (RMNPs) in an oxygen (60%)−argon (40%) atmosphere by exploiting an ultrasonic levitator with droplets ignited by a carbon dioxide laser. Ultraviolet−visible (UV−vis) emission spectroscopy revealed the presence of gas-phase aluminum (Al) and titanium (Ti) atoms. These atoms can be oxidized in the gas phase by molecular oxygen to form spectroscopically detected aluminum monoxide (AlO) and titanium monoxide (TiO) transients. Analysis of the optical ignition videos supports that the nanoparticles are ignited before JP-10. The detection of boron monoxide (BO) further proposes an active surface chemistry through the oxidation of the RMNPs and the release of at least BO into the gas phase. The oxidation of gas-phase BO by molecular oxygen to boron dioxide (BO_2) plus atomic oxygen might operate in the gas phase, although the involvement of surface oxidation processes of RMNPs to BO_2 cannot be discounted. The UV−vis emission spectra also revealed the key reactive intermediates (OH, CH, C_2, and HCO) of the oxidation of JP-10. Electronic structure calculations reveal that the presence of reactive radicals has a profound impact on the oxidation of JP-10. Although titanium monoxide (TiO) reacts to produce titanium dioxide (TiO_2), it does not engage in an active JP-10 chemistry as all abstraction pathways are endoergic by more than 217 kJ mol^{-1}. This is similar for atomic aluminum and titanium, whose hydrogen abstraction reactions from JP-10 were revealed to be endoergic by at least 77 kJ mol^{-1}. Therefore, aluminum and titanium react preferentially with molecular oxygen to produce their monoxides. However, the formation of BO, AlO, and BO_2 supplies a pool of highly reactive radicals, which can abstract hydrogen from JP-10 via transition states ranging from only 1 to 5 kJ mol^{-1} above the separated reactants, forming JP-10 radicals along with the hydrogen abstraction products (boron hydride oxide, aluminum monohydroxide, and metaboric acid) in the overall exoergic reactions. These abstraction barriers are well below the barriers of abstractions for ground-state atomic oxygen and molecular oxygen. In this sense, gas-phase BO, AlO, and BO_2 catalyze the oxidation of gas-phase JP-10 via hydrogen abstraction, forming highly reactive JP-10 radicals. Overall, the addition of RMNPs to JP-10 not only provides a higher energy density fuel but is also expected to lead to shorter ignition delays compared to pure JP-10 due to the highly reactive pool of radicals (BO, AlO, and BO_2) formed in the initial stage of the oxidation process.

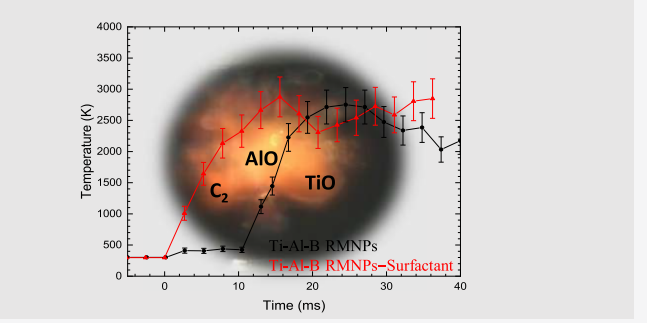

1. INTRODUCTION

Contemporary combustion processes in air-breathing propulsion systems rely on the oxidation of hydrocarbon-based fuels such as Jet Propellant-10 (JP-10). *exo*-Tetrahydrodicyclopentadiene ($C_{10}H_{16}$; Figure 1) represents a single-component hydrocarbon fuel and is the dominant constituent of JP-10 that is exploited in detonation engines, missiles, and supersonic combustion ramjets.[1−4] With attractive properties such as high thermal stability and a volumetric energy density close to 40 kJ cm^{-3} when completely oxidized, JP-10 has drawn extensive attention from the experimental, theoretical, and modeling communities[5−41] to examine the features of thermal decom-

Received: September 21, 2021
Revised: December 2, 2021
Published: December 22, 2021

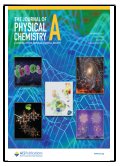

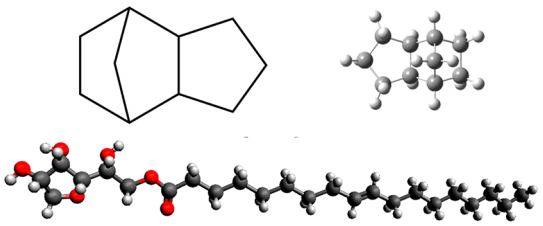

Figure 1. Molecular structure of JP-10 (top) and the surfactant (bottom). Carbon, hydrogen, and oxygen atoms are color-coded in black, white, and red, respectively.

position and the mechanisms of oxidation. Exploiting shock tubes,[37] flow tubes,[7,8,17,18] and high-temperature chemical reactors,[9,10,13,16] a detailed understanding of the decomposition (pyrolysis) of JP-10 is beginning to emerge. This unimolecular decomposition leads to smaller C2−C9 hydrocarbon molecules and reactive transient species, with aliphatic radicals, resonantly stabilized free radicals, and aromatic radicals among them,[42] which initiate and drive the complex chemistry of the oxidation of JP-10-based jet fuel. This initial decomposition chemistry,[43] which has been suggested to be temporarily uncoupled from the oxidation stage at least in the absence of metal catalysts,[44] is often dubbed as delivering the building blocks for the oxidation of JP-10.

However, concerns on the limited volumetric energy density of the traditional hydrocarbon fuel of only up to 40 kJ cm^{-3}, which severely constrains the range and hence the performance of air-breathing propulsion systems, are growing. The development of the next generation of air-breathing propulsion systems requires a fuel with higher energy per volume and higher molecular weight than that of traditional hydrocarbon fuel. This necessitates the development of the next generation of high-energy-density fuels and high-energy-density fuel additives,[45−51] ultimately enhancing the performance and range of air-breathing propulsion systems. High-energy-density fuel additives based on reactive metal nanopowders (RMNPs) hold promise in air-breathing engine applications. However, there is currently an incomplete understanding of the underlying elementary mechanisms involved in the oxidation of RMNPs-doped hydrocarbon-based fuel such as JP-10. Boron holds the highest energy density of 138 kJ cm^{-3} compared to other combustible metals such as aluminum (84 kJ cm^{-3}) or magnesium (43 kJ cm^{-3}). However, the refractory nature of boron, which is reflected in the high melting and boiling points of 2349 and 4,200 K, respectively, makes it difficult to ignite and prevents it from gasification during combustion. The Ti−Al−B-RMNPs are a demonstration of an approach to harness boron combustion, where boron is mixed with reactive metals such as titanium and aluminum, providing more favorable combustion characteristics. Titanium and aluminum undergo exoergic reactions with boron-forming borides such as aluminum diboride (AlB_2) and titanium diboride (TiB_2).[52−54] This has the potential to heat up the RMNPs to temperatures at which boron oxidation can readily occur, thus relieving the complications of kinetic trapping of boron as metaboric acid (HOBO), which prevents the full energy release. Therefore, RMNPs containing titanium, aluminum, and boron represent a new class of high-energy-density fuel additives with a volumetric energy content exceeding 89 kJ cm^{-3}. Epshteyn et al. proposed RMNPs prepared through sonochemically mediated dehydrogenation of *in situ*-generated complex metal hydrides[55] as promising fuel additives due to their high specific surface area, high energy density, and potential catalytic capability.[52−54,56−60] The authors demonstrated that RMNPs containing titanium (Ti), aluminum (Al), and boron (B) in JP-5 at concentrations of up to 4% by weight resulted in shorter ignition delays of the hydrocarbon, that is, the period between the beginning of the fuel injection into an engine cylinder and the beginning of combustion, and increased burn durations.[61] The RMNP additives resulted in an increase of nitrogen oxides, carbon dioxide, and carbon monoxide and a simultaneous oxygen decrease in the exhaust compared to results with pure JP-5 as a reference system. As revealed in the combustion studies of RMNPs in decane liquid fuel spray burners,[57,61] the exploitation of RMNPs overcomes traditional problems encountered with metal nanoparticles, that is, a passivation layer of oxides that reduces the active metal content since the oxide shell becomes an increasing portion of the overall fuel mass as the particle size is reduced, which in turn has the potential to significantly increase the overall volumetric energy density of the fuel.[45,62−64]

However, the underlying mechanisms in the oxidation of mixed, multimetal RMNPs have not been comprehensively unraveled to date. Considering this lack of detailed knowledge, the objectives of the present work are to investigate the oxidation of acoustically levitated droplets of JP-10 doped with 2 wt % titanium (Ti)−aluminum (Al)−boron (B)-based RMNPs (system a) in an atmosphere of 60% oxygen and 40% argon with the oxidation initiated by a carbon dioxide laser. It shall be stressed that under these conditions, droplets of pure JP-10 in the absence of metal powder additives did not ignite but instead evaporated prior to their ignition.[65] We also explore the effects of adding 1 wt % surfactant (Span80) to the JP-10-RMNP droplet (system b) on the oxidation process including, for example, ignition delay and maximum flame temperature. JP-10 droplets doped with 2 wt % aluminum (Al) (system c) and 2 wt % aluminum (Al) along with 1 wt % surfactant (Span80) (system d) serve as the baseline systems to determine the improvements in the combustion compared to the more traditional single-metal additive Al and investigate the effects of the sorbitan monooleate.[65−68] These experiments are complemented by the electronic structure calculations exploring the initial steps on the formation of JP-10-based hydrocarbon radicals accessed through hydrogen abstraction pathways by molecular oxygen (O_2, $X^3\Sigma_g^-$), atomic oxygen [$O(^3P_j)$], and oxides [$BO(X^2\Sigma^+)$; $AlO(X^2\Sigma^+)$; $TiO(X^3\Delta)$; and $BO_2(X^2\Sigma_g^+)$] formed during the oxidation of the RMNPs to gauge the effect of Ti−Al−B-based RMNPs on the oxidation of JP-10.

2. EXPERIMENTAL METHODS

2.1. Materials. JP-10 ($C_{10}H_{16}$, ≥98%), the sorbitan monooleate surfactant ($C_{24}H_{44}O_6$-Span 80) (Figure 1), and aluminum nanoparticles (Al NPs) with diameters of 251 ± 36 nm were purchased from BOC Science, Sigma-Aldrich, and NovaCentrix, respectively. The RMNPs were synthesized in-house via the previously published procedure utilizing the sonochemically mediated decomposition of unstable mixed-metal hydrides of Ti, Al, and B generated in situ; the specific procedure involved the "reverse" addition with a thermal vacuum treatment performed at 373 K, but the reaction was performed on an approximately 3-fold increased scale.[55] The resultant RMNPs were found to exhibit an average particle size of 160 ± 80 nm, as determined via dynamic light scattering with a Ti/Al:B atomic ratio of approximately 1:2:6. Two distinct RMNP-loaded JP-10 samples were prepared by mixing JP-10 with (a) 2 wt % Ti−Al−B-based RMNPs (JP-10-RMNPs) and

https://doi.org/10.1021/acs.jpca.1c08335
J. Phys. Chem. A 2022, 126, 125−144

with (b) 2 wt % Ti−Al−B-based RMNPs along with 1 wt % Span80 (JP-10-RMNPs−surfactant). We also prepared two reference systems of JP-10 samples by mixing JP-10 with (c) 2 wt % aluminum (Al) (JP-10-Al) and (d) 2 wt % aluminum (Al) with 1 wt % surfactant (Span80) (JP-10-Al−surfactant). Without the surfactant, the RMNPs did not disperse uniformly within JP-10. However, the addition of the surfactant essentially eliminated particle agglomeration, and the RMNPs were uniformly dispersed and suspended in JP-10. The samples were sonicated using a benchtop ultrasonic cleaning bath (Branson 3510:115 V AC, 10 min) immediately prior to each experiment to ensure that no separation between the particles and the liquid takes place during the experiments.

2.2. Acoustic Levitation Apparatus and Characterization Techniques. The oxidation process for single, levitated JP-10 droplets doped with Ti−Al−B-based RMNPs (hereafter, Ti−Al−B-RMNPs) was explored experimentally by utilizing an ultrasonic levitation device as described in refs 66, 69−71 in detail. Briefly, the core of the levitator comprises a piezoelectric transducer operating at an oscillation frequency of 58 kHz along with a concave shape reflector. In a gaseous medium, a standing wave is generated through the reflection of the ultrasonic soundwaves between the transducer and the reflector. The acoustic radiation pressure counterbalances the gravitational force and therefore levitates the droplet slightly below one of the pressure minima of the standing wave. The ultrasonic levitator is housed in a pressure-compatible stainless-steel process chamber, which enables the levitated droplet to be studied in distinct gas(eous) environments (inert, toxic, and/or reactive) over a pressure range from a few tens of Torr up to 1500 Torr, although in principle, higher operational pressures are sustainable. Here, droplets were levitated in an environment of 60% oxygen (O_2, 99.9999%, Airgas) and 40% argon (Ar, 99.9999%, Airgas) at a total pressure of 860 ± 1 Torr. The droplets were oblate spheroids with average horizontal and vertical diameters of 2.6 ± 0.2 mm and a mean vertical diameter of 1.4 ± 0.2 mm, leading to a typical droplet volume of 5 ± 1 mm^3, where the uncertainties represent how accurately we could control the size of the droplets for repeated droplet depositions. The droplets were injected into the pressure node through a homemade droplet deposition system comprising a micro needle, a wobble stick, and polyetheretherketone tubing, which connects the needle to a syringe located on the outside of the process chamber. After the stabilization of the droplet, levitated droplets of systems (a,b) as defined in section 2 were then heated by the output of a carbon dioxide (CO_2) laser emitting at a wavelength of 10.6 μm. A planar copper mirror and zinc selenide (ZnSe) windows on the chamber were used to transport the infrared beam to the levitated particle, which is located 104 cm from the exit of the laser as measured along the path of the beam. The diameter of the beam exiting the laser is 2.5 ± 0.5 mm ($1/e^2$) and the beam divergence (full angle) is less than 7.0 mR. By using an 8× beam expander followed by a copper parabolic mirror with a focal length of 300 mm, the laser beam was focused to a diameter of 0.2 mm on the droplet.[66,69] The laser output can be tuned to between 1 and 40 W; the present experiments were conducted at an output power of 32 W, which was achieved by setting the duty cycle of the laser to 80%.

Prior to the ignition, the doped JP-10 droplets were characterized spectroscopically via Raman and Fourier transform infrared (FTIR) spectroscopy.[65,66,69] Raman transitions were excited by the 532 nm line of a diode-pumped, Q-switched Nd:YAG laser (CrystaLaser; model QL532-1W).

The penetration depth δ of the laser is defined as the depth at which the power of the light decreases to 1/e of its value; this can be calculated via $\delta = \lambda/4\pi\kappa$, where λ is the wavelength of the light (532 nm) and κ is the imaginary part of the complex refractive index of the material. For JP-10, κ is 1.48 for 532 nm. This gives a penetration depth of the Raman diagnostic of 29 nm.

At a typical pulse repetition rate of 1 kHz, the average power output is 200 mW and the pulse width is 13.5 ns. The laser beam was directed into the chamber through an antireflection coated window after deflection from a 45° mirror (Edmund Optics; model NT45-991, >99% reflectance) and a 45° dichroic beam splitter (Semrock; RazorEdge, model LPD01-532RU-25 × 36 × 2.0). A plano-convex lens with a focal length of 60 mm focuses the laser beam onto the sample and subsequently collimates the Raman-shifted photons which were backscattered from the levitated droplet. Although the dichroic beam splitter reflected the incident 532 nm laser beam toward the sample, it transmitted the longer Raman-shifted wavelengths of the backscattered photons. After passing through a 532 nm RazorEdge ultrasteep long-pass edge filter (Semrock; model LP03-532RE-25), which further minimizes the elastically scattered 532 nm laser light, a 50 mm f/1.8 camera lens (Nikon; Nikkor 2137) focuses the backscattered beam through the entrance slit of the spectrograph. The slit width of 100 μm results in a wavenumber resolution of 9 cm^{-1}. The light then enters a Holospec f/1.8 imaging spectrometer (Kaiser optical systems; model 2004500-501), where the diverging beam is collimated by a lens toward two overlaid holographic transmission gratings (Kaiser Optical Systems; Model Holoplex HPG-532). One grating disperses the low Raman-shift wavenumbers from 2388 to 168 cm^{-1}, whereas the other separates the higher Raman shifts in the 4387−2265 cm^{-1} range. The gratings simultaneously disperse light from the two Raman-shift ranges onto spatially distinct halves of a Peltier-cooled charge-coupled device (CCD) detector kept at 255 K (Princeton Instruments, PI-MAX2), which is composed of 1024 × 256 pixels each with a pixel size of 26 μm.

To reduce the fluorescence background and enable the spectra to be collected in bright light conditions, the pulsed laser described above and a gated detector are employed. To detect the faster Raman signal while rejecting most of the longer-lived fluorescence, we optimized the time delay between the laser pulse and opening the gate to collect the CCD signal (gate delay) and the period for which the gate is open (period). In the present setup, the CCD is open for 50 ns with a gate delay of 480 ns ($T = T_0 + 480$ ns). The repetition rate of the above procedure was controlled by a Quantum Composers (model 9518+) pulse generator, which produced 1 μs wide TTL outputs from its channels A and B to trigger the CCD controller and laser, respectively, at a rate adjustable between approximately 100 Hz and 8 kHz.[72] Peak assignments were based on scaled computational normal modes of JP-10 (Figure S7).[73] The Raman shift scale was calibrated using cyclohexane, toluene, and acetonitrile as described in the Supporting Information (Figure S8).

The ignition and oxidation processes of JP-10 in the presence of RMNPs (system a) and RMNPs−surfactant (system b) were characterized by using Ultraviolet−visible (UV−vis) and FTIR spectroscopy along with a high-speed optical camera and an IR thermal imaging camera. UV−vis emission spectra of the flames were collected to identify the radical intermediates, individual atoms, and molecules formed during the oxidation processes, whereas the FTIR transmission spectra of the gases produced

https://doi.org/10.1021/acs.jpca.1c08335
J. Phys. Chem. A 2022, 126, 125−144

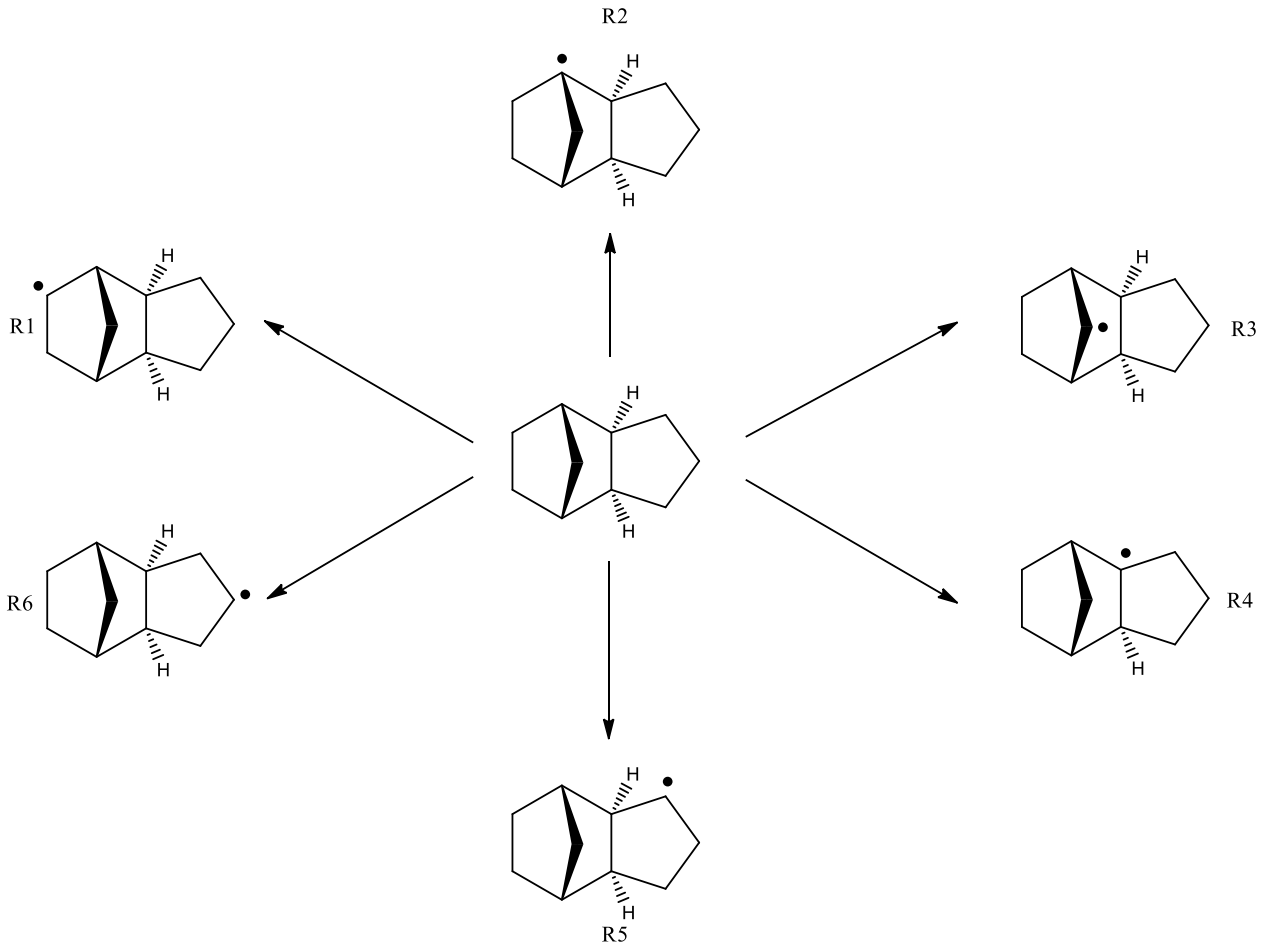

Figure 2. JP-10-based radicals generated via C−H bond cleavages in JP-10.

after the combustion were recorded to identify the terminal oxidation products. The UV−vis spectra were recorded using a StellarNet SILVER-Nova UV−vis spectrometer combined with a fiber optic probe. The fiber optic probe was aligned on the droplet at a distance of approximately 6 mm using an *x*, *y*, *z* manipulator. For UV−vis emission spectroscopy, the UV−vis emissions from the igniting droplet were collected by the read fiber, exited the chamber via a ConFlat fiber optic feedthrough, and finally were dispersed within the UV−vis spectrometer, which is sensitive over a wavelength range from 200 to 1,100 nm and has a spectral resolution of 2 nm. FTIR transmission spectra were collected with the help of a Nicolet 6700 FTIR spectrometer over the wavelength range of 500−5000 cm^{-1} with two stages of copper mirror optics to probe gases evolved during the ignition event.

Optical videos of these high-speed ignition events were captured by a Phantom Miro 3a10 camera (Supporting Information; Movies M1 and M2) equipped with a Navitar Zoom 6000 modular lens system at a rate of 1 kHz. Additionally, thermal imaging videos of the ignition process were collected by an FLIR A6703sc infrared camera, which were converted to temporal plots of the maximum temperature within the 10 mm × 8 mm field of view (FOV). The temperature temporal profiles enable some of the key features of the combustion process to be examined, for example, the ignition delay time, the maximum flame temperature (T_{max}), and the burn rates. The emissivity of the flames ε is required to place the uncalibrated temperatures from the IR camera on an absolute scale. The emissivity was deduced by fitting a gray body distribution to the background in the UV−vis spectrum and then comparing the resulting absolute temperature with the uncalibrated value obtained from an infrared thermal video of the same ignition process. The resulting value for the emissivity of 0.115 was applied only at temperatures above the autoignition temperature of JP-10, that is, 509 K.

3. COMPUTATIONAL METHODS

Reaction energetics involving the atoms (B, Al, and Ti) and oxides (BO, AlO, TiO, and BO_2) were computed in Gaussian09[74] with spin-projected MP2[75] and the 6-311g* basis set.[76−78] For comparison, the reaction, product, and transition state energies for hydrogen abstraction from JP-10 to AlO were computed at a single site using MP2 with the larger def2-TZVP[79] basis set, which did not result in significantly different relative energies or geometries. The overall reaction energies for hydrogen abstraction to the atoms and oxides were also computed using the density functional theory (DFT) with the B3LYP[80−82] functional, including Grimme's D3[83] empirical dispersion correction, and the def2-TZVP basis set (B3LYP-D*/def2-TZVP). Various trial structures for JP-10 were built by hand and optimized to an energy minimum. The lowest-energy structure after the optimization was used as the starting point for all subsequent calculations. In most reactions, stable, non-covalently bound van der Waals (vdW) complexes occurred on either side of the transition state. To find these complexes, a series of trial structures were generated, optimized to an energy

https://doi.org/10.1021/acs.jpca.1c08335
J. Phys. Chem. A 2022, 126, 125−144

Table 1. Reaction Energies Computed at the MP2/6-311g*, B3LYP-D*/def2-TZVP, B3LYP/6-311G, and G3 Levels of Theory**

	reaction energy,[a] kJ mol^{-1}	reaction energy,[b] kJ mol^{-1}	reaction energy,[c] kJ mol^{-1}	reaction energy,[d] kJ mol^{-1}
R1	371	396	394	400
R2	409	433	422	437
R3	393	418	415	423
R4	378	399	395	406
R5	367	390	388	397
R6	370	391	390	399

[a]MP2/6-311g*. [b]B3LYP-D*/def2-TZVP levels involved in carbon−hydrogen bond cleavages in JP-10 leading to six distinct hydrocarbon radicals, R1 to R6 (Figure 2), compared with previous calculations. [c]B3LYP/6-311G**. [d]G3. All energies include ZPE corrections.

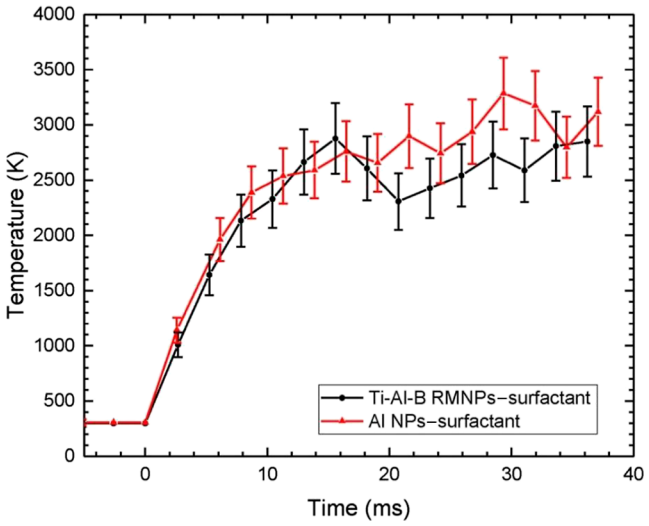

Figure 3. Temperature temporal profiles produced by igniting a JP-10 droplet for systems (b) [Ti−Al−B RMNPs−surfactant] and (d) [Al NPs−surfactant]. The laser irradiation started at t = 0 ms.

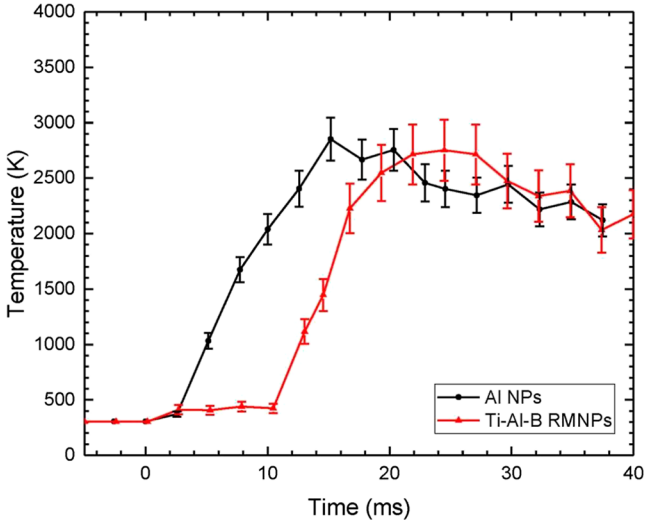

Figure 4. Temperature temporal profiles produced by igniting a JP-10 droplet for systems (a) [Ti−Al−B RMNPs] and (c) [Al NPs]. The laser irradiation started at t = 0 ms.

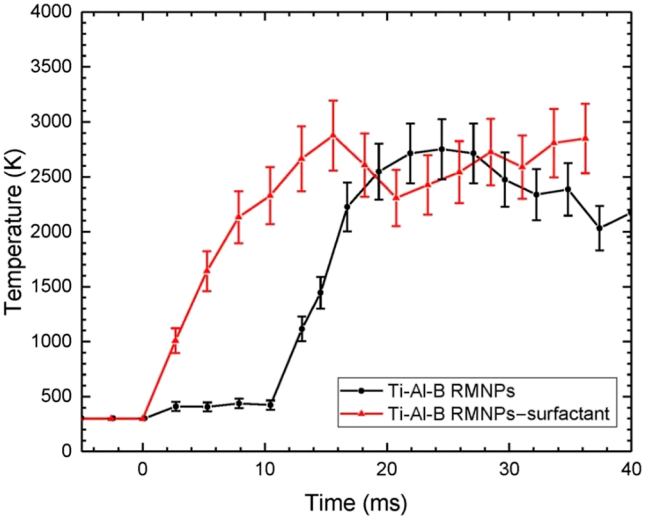

Figure 5. Temperature temporal profiles produced by igniting a JP-10 droplet for systems (a) [Ti−Al−B RMNPs] and (b) [Ti−Al−B RMNPs−surfactant]. The laser irradiation started at t = 0 ms.

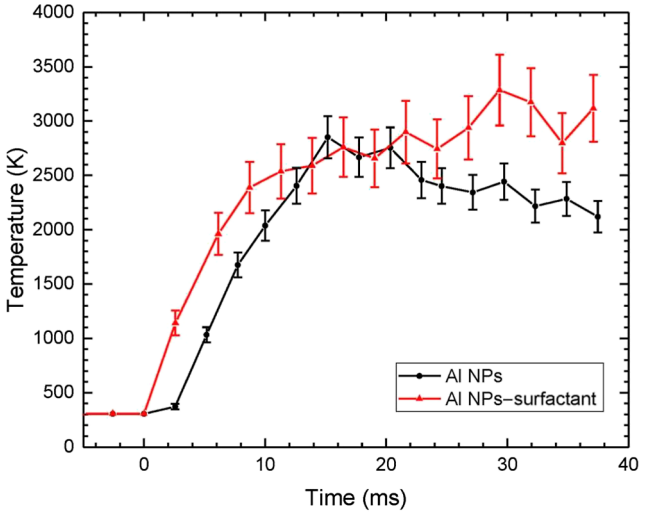

Figure 6. Temperature temporal profiles produced by igniting a JP-10 droplet for systems (c) [Al NPs] and (d) [Al NPs−surfactant]. The laser irradiation started at t = 0 ms.

minimum, and discarded if they did not converge to a relevant geometry. Initial estimates for transition states were generated from these noncovalently bound intermediates using the geometric velocity method[84] and refined with a combination of saddle-point[85] and synchronous transit-guided quasi-Newton[86,87] optimizations. Our attempts to model hydrogen abstraction to metal-containing complexes with the DFT in the def2-TZVP basis set found that both the B3LYP and PBE[88,89] functionals significantly underestimated the transition state barriers; adding a D3 empirical dispersion correction did not remedy this. The use of MP2, which is well-suited to capturing dynamical electron correlation effects, remedied both of these problems. Energies for carbon−hydrogen bond cleavages in JP-10, leading to six distinct hydrocarbon radicals from R1 to R6 (Figure 2), were computed using MP2/6-311g* B3LYP-D*/def2-TZVP. These values were compared to previous calculations at the B3LYP/6-311G** and G3 levels (Table 1).[42] Deviations between the B3LYP-D*/def2-TZVP results and both sets of previous calculations are less than 5 kJ

https://doi.org/10.1021/acs.jpca.1c08335
J. Phys. Chem. A 2022, 126, 125−144

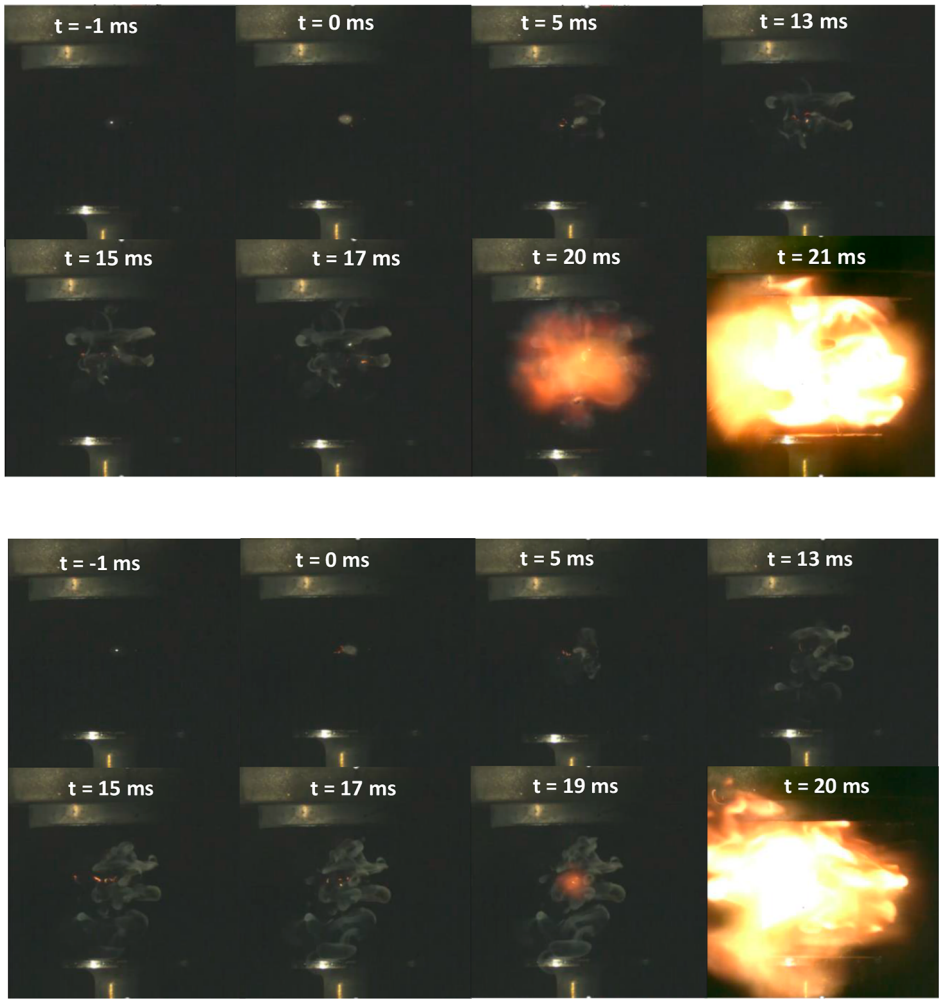

Figure 7. Sequence of two high-speed video images of the ignition of JP-10 Ti−Al−B RMNPs−surfactant droplets acquired at a frame rate of 1 kHz. t = 0 ms represents the time at which the carbon dioxide laser hit the droplet. Movies M1 and M2 can be retrieved from the Supporting Information. In these videos, ignition events are delayed to about 20 ms.

mol^{-1}. The small discrepancies with the previous B3LYP calculations are likely due to the fact that the present work uses a significantly larger basis. Additionally, the previous work did not include an empirical dispersion correction, although this should have had a minimal impact on hydrogen abstraction energies due to the lack of noncovalent interactions.

The reactions of O (^{3}P) + JP-10 → JP-10 radicals (R1−R6) + OH and O_2 + JP-10 → JP-10 radicals (R1−R6) + O_2H were explored on adiabatic triplet ground-state potential surfaces. The transition states that lead to vdW complexes in the exit channels and products, JP-10 radicals and OH or O_2H, are identified and characterized utilizing B3LYP[80,81,90,91]/cc-pVTZ calculations to obtain the optimized geometries and harmonic vibrational frequencies, except for R2(TS), R4(TS), R2-OOH, and R4-OOH, which were located at the MP2/cc-pVDZ level of theory. Their energies are further refined at the CCSD[92−95]/cc-pVTZ level of theory with B3LYP/cc-pVTZ zero-point energy corrections. The Gaussian16 program[96] was employed in the electronic structure calculations.

4. RESULTS AND DISCUSSION

4.1. Raman and FTIR Spectroscopy. The Raman and FTIR spectra of pure JP-10 are dominated by fundamental modes of the JP-10 molecule covering CH/CH_2 stretching modes (2865−2954 cm^{-1}); CH_2 scissor modes (1444−1463 cm^{-1}); CH/CH_2 rocking, bending, twisting, and wagging modes (1030−1420 cm^{-1}); carbon−carbon stretching, rocking, and bending modes (188−980 cm^{-1}); and ring twisting, rocking, and stretching modes (Figures S3−S10 and Table S1). Upon the addition of Al NPs, the peaks shift by only 2 cm^{-1} at most; this is within the resolution of the Raman spectra. However, the addition of the JP-10-Ti−Al−B NPs changed the Raman spectra in various aspects. First, as evident from Table S1, various fundamentals are red-shifted by up to 14 cm^{-1} due to the intermolecular forces between the JP-10 molecules and the surfaces of the Ti−Al−B NPs. Second, the υ_{10} mode, which is Raman inactive, becomes Raman active in the JP-10-Ti−Al−B NP system. Third, two additional peaks at 227 cm^{-1} (ν_A) and 267 cm^{-1} (ν_B) can be linked to Al−B and Ti−B stretching modes of aluminum borides and titanium borides, which were also observed in the pure Ti−Al−B NPs (Figures S3−S8).[73,97−109] We did not detect any evidence of features associated with titanium aluminides. This might be due to the fact that titanium and aluminum resemble less prominent components of the boron-dominated RMNPs (Ti/Al/B = 1:2:6) or that Ti and Al form stronger bonds with boron.

It should be highlighted that in order to record the Raman spectra, the 532 nm laser beam, which has a diameter of about

https://doi.org/10.1021/acs.jpca.1c08335
J. Phys. Chem. A 2022, 126, 125−144

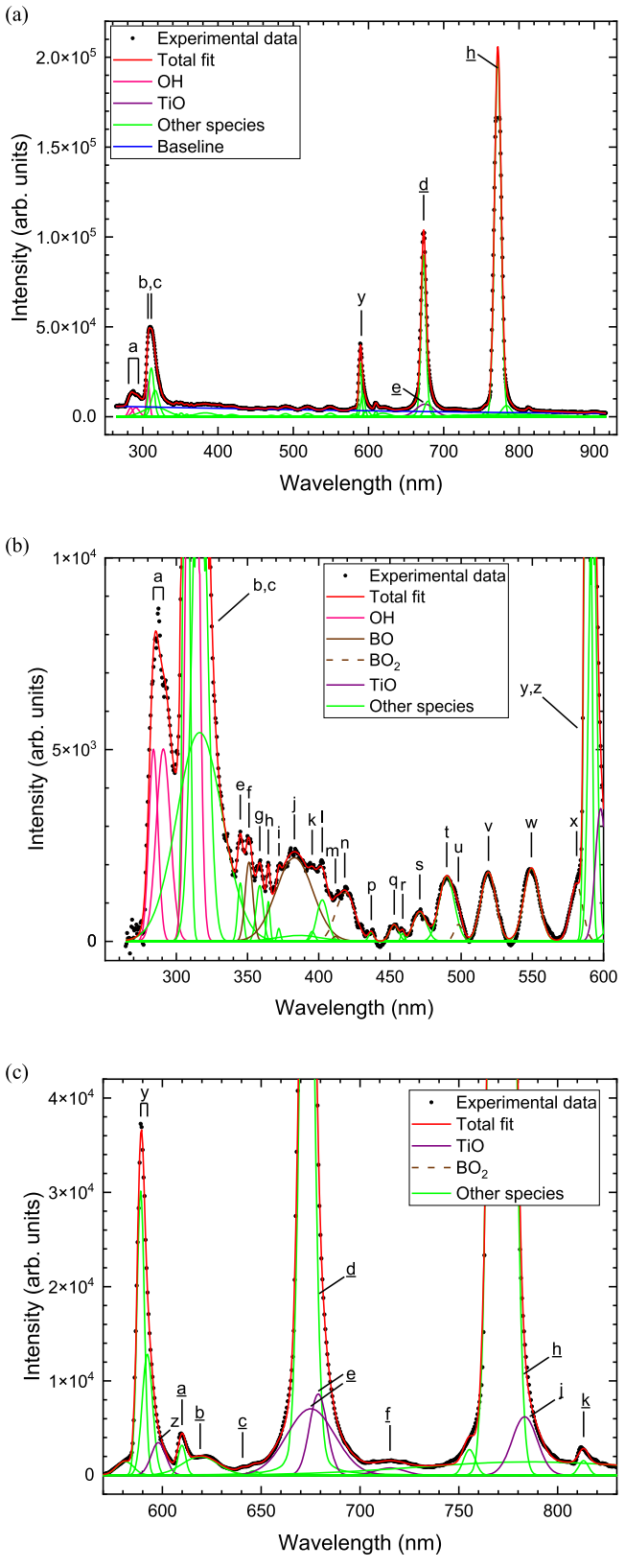

Figure 8. (a) UV−vis emission spectrum produced during the ignition of a JP-10 droplet containing Ti−Al−B nanoparticles initially levitated in 60% O_2 and 40% Ar. The total fit (red line) was obtained by simultaneously optimizing 43 peaks plus the background (blue line). Unique emissions of OH, TiO, BO, and BO_2 are color-coded in pink, purple, brown, and brown-dashed, respectively. (b,c) Zoomed-in spectra. The assignments of bands (a−k) are presented in Table 2.

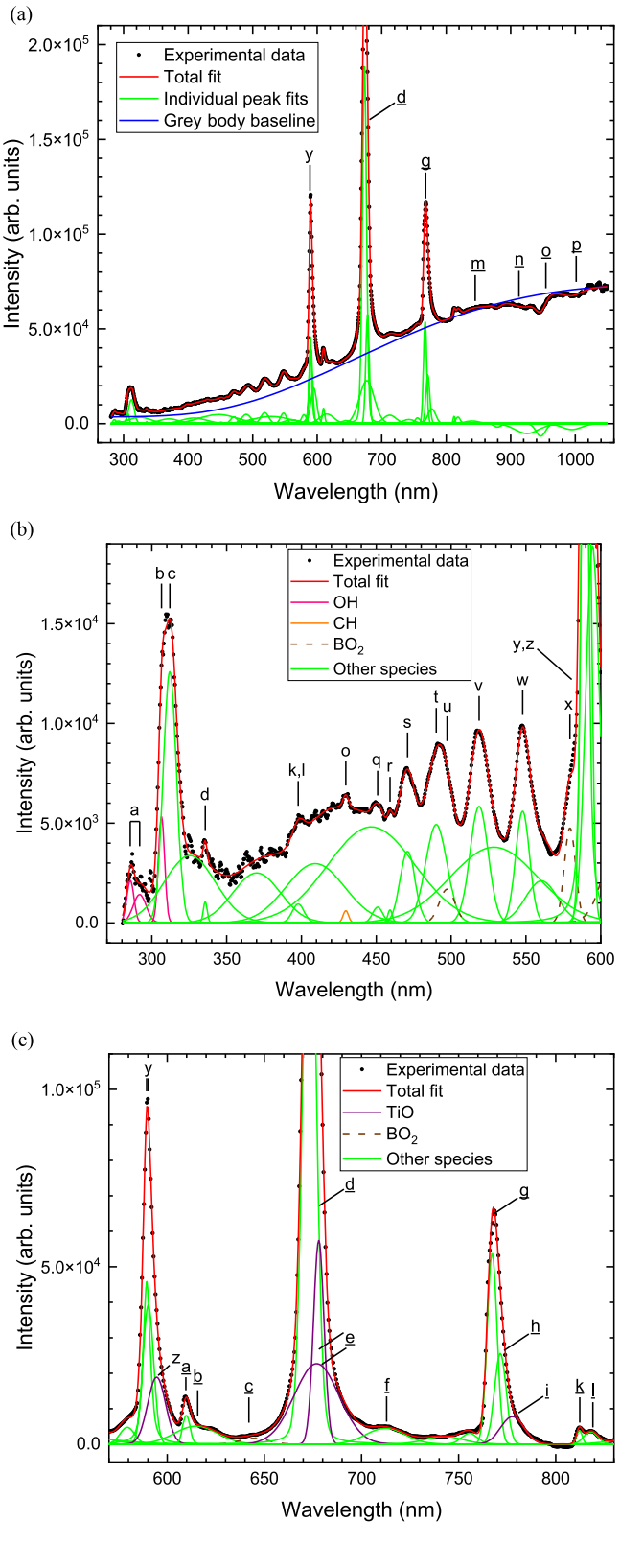

Figure 9. (a) UV−vis emission spectrum produced during the ignition of a JP-10 droplet containing Ti−Al−B nanoparticles coated with the surfactant sorbitan monooleate initially levitated in 60% O_2 and 40% Ar. The total fit (red line) was obtained by simultaneously optimizing 43 peaks plus the background (blue line). Unique emissions of OH, TiO, BO, and BO_2 are color-coded in pink, purple, brown, and brown-dashed, respectively. (b,c) Zoomed-in spectra. The assignments of bands (a−l) are presented in Table 2.

https://doi.org/10.1021/acs.jpca.1c08335
J. Phys. Chem. A 2022, 126, 125−144

Table 2. Vibrational Mode and Electronic Transition Assignments for the Bands or Peaks in the UV−Vis Emission Spectrum Produced during the Ignition of a JP-10 Droplet Containing Ti−Al−B Nanoparticles when Levitated in 60% O_2 and 40% Ar[j]

peak or band	peak wavelength or band center (nm)[a]	peak wavelength or band center (nm)[a] with Span80	molecule, atom, or radical	ref. wavelength (nm)	transition	branch; vibrational quantum numbers: (ν', ν'') or (ν_1',ν_2', ν_3')−(ν_1'',ν_2'',ν_3'')
a	283.9 290.9 ± 2.9	285.6 291.9 ± 4.8	OH	281.1−282.9[b]	A $^2\Sigma^+$−X $^2\Pi$	R_1, R_2, Q_1, Q_2; (1, 0)
				287.5−289.3[b]	A $^2\Sigma^+$−X $^2\Pi$	R_1, R_2, Q_1, Q_2; (2, 1)
				294.5−296.2[b]	A $^2\Sigma^+$−X $^2\Pi$	R_1, R_2, Q_1, Q_2; (3, 2)
b	307.0	306.5	OH	306.4−309.0[b]	A $^2\Sigma^+$−X $^2\Pi$	R_1, R_2, Q1, Q_2; (0, 0)
c	311.4	312.0	Al	309.3[c]	$3s^23p^2P$−$3s^23d^2D$	R_1, R_2, Q_1, Q_2; (1, 1)
			OH	312.2−314.7[b]	A $^2\Sigma^+$−X $^2\Pi$	
d		335.7	HCO	337.6[b]	A_1	(0, 14)
			O_2	337.0[b]	$B^3\Sigma_u^-$−$X^3\Sigma_g^-$	
e	344.9		K	344.6−344.7[c]	$3p^64s\ ^2S$−$3p^66p\ ^2P°$	
f	351.0		BO	351.1[b]	A $^2\Pi$−X $^2\Sigma^+$	(4, 0)
g	358.6		HCO	358.8[b]	A_1	
h	364.6		Ti	363.5−365.3[c]	$3d^24s^2\ ^3F$−$3d^2(^3F)4s4p(^1P°)^3G°$	(3, 0)
			K	364.9[c]	$3p^64\ s\ ^2S$−$3p^64d\ ^2D$	
			BO	366.2[b]	A $^2\Pi$−X $^2\Sigma^+$	
i	372.0		Ti	∼375[c]	$3d^24s^2\ ^3F$−$3d^2(^1D)4s4p(^3P°)\ ^3F°$	
j	382.9 ± 2.2		BO	383.0[b]	A $^2\Pi$−X $^2\Sigma^+$	(2, 0)
k	395.4 ± 3.1	397.8 ± 1.3	Al	394.4−396.2[c]	$3s^23p\ ^2P°$−$3s^24s\ ^2S$	
			Ti	394.9−395.8[c]	$3d^24s^2\ ^3F$−$3d^3(^4F)4p\ ^3D°$	
l	402.5 ± 2.2	397.8 ± 1.3	Ti	398.2−399.9[c]	$3d^24s^2\ ^3F$−$3d^2(^3F)4s4p(^1P°)$	R_{21}, R_1, R_2, Q_1; (1, 0)
			BO	401.5−403.7[b]	A $^2\Pi$−X $^2\Sigma^+$	
			K	404.4−404.7[c]	$3p^64s\ ^2S$−$3p^65p\ ^2P°$	
m	411.7 ± 3.8		BO	412.4[b]	A $^2\Pi$−X $^2\Sigma^+$	(2, 1)
n	418.3 ± 1.4		BO_2	416.9−416.3[d]	A $^2\Pi_u$−X $^2\Pi$g	R_1, R_2; (0, 2, 2)−(0, 0, 0)
o		429.6 ± 1.0	CH	431.4[b]	A $^2\Delta$−X $^2\Pi$	Q; (0,0)
p	436.9 ± 1.5		BO	433.9−436.6[b]	A $^2\Pi$−X $^2\Sigma^+$	R_{21}, R_1, R_2, Q_1; (1, 1)
			C_2	436.5[b,e]	d $^3\Pi_g$−a $^3\Pi$u	(4, 2)
			C_2	437.1[b,e]	d $^3\Pi_g$−a $^3\Pi$u	(3, 1)
			C_2	438.2[b,e]	d $^3\Pi_g$−a $^3\Pi$u	(2, 0)
q	453.0 ± 1.5	450.9 ± 1.5	BO_2	450.3−450.6[d]	A $^2\Pi_u$−X $^2\Pi^g$	R_1, R_2; (1, 6, 0)−(0, 0, 0)
			BO_2	449.7−450.3[d]	A $^2\Pi_u$−X $^2\Pi^g$	R_1, R_2; (2, 4, 0)−(0, 0, 0)
			AlO	453.8[b]	A $^2\Sigma^+$−X $^2\Sigma^+$	(5, 3)
r	459.0 ± 1.7	459.2 ± 1.1	BO	458.6−461.5[b]	A $^2\Pi$−X $^2\Sigma^+$	R_{21}, R_1, R_2, Q_1; (0, 1)
			Li	460.3[c]	$1s^22p\ ^2P°$−$1s^24d\ ^2D$	
s	471.0	470.9	AlO	467.2[b]	A $^2\Sigma^+$−X $^2\Sigma^+$	(2, 1)
			AlO	469.5[b]	A $^2\Sigma^+$−X $^2\Sigma^+$	(3, 2)
			BO_2	466.6−469.5[d]	A $^2\Pi_u$−X $^2\Pi_g$	R_1, R_2; (2, 2, 0)−(0, 0, 0)
			BO_2	470.4−472.7[d]	A $^2\Pi_u$−X $^2\Pi_g$	R_1, R_2; (1, 4, 0)−(0, 0, 0)
			C_2	469.8[b,e]	d $^3\Pi_g$−a $^3\Pi_u$	(3, 2)
			C_2	471.5[b,e]	d $^3\Pi_g$−a $^3\Pi_u$	(2, 1)
			C_2	473.7[b,e]	$d^3\Pi_g$−a $^3\Pi_u$	(1, 0)
			BO	471.9[b]	A $^2\Pi$−X $^2\Sigma^+$	(1, 2)
t	489.9 ± 2.0	490.1 ± 1.2	AlO	486.6[b]	A $^2\Sigma^+$−X $^2\Sigma^+$	(1, 1)
			AlO	488.9[b]	A $^2\Sigma^+$−X $^2\Sigma^+$	(2, 2)
			BO_2	490.7−491.7[d]	A $^2\Pi_u$−X $^2\Pi_g$	R_1, R_2; (1, 2, 0)−(0, 0, 0)
			BO_2	492.9−494.1[d]	A $^2\Pi_u$−X $^2\Pi_g$	R_1, R_2; (2, 0, 0)−(0, 0, 0)
u	498.1 ± 2.5	497.3 ± 3.1	BO_2	496.5−497.4[d]	A $^2\Pi_u$−X $^2\Pi_g$	R_1, R_2; (0, 4, 0)−(0, 0, 0)
v	519.2	518.7	C_2	516.5[b,e]	d $^3\Pi_g$−a $^3\Pi_u$	(0, 0)
			BO_2	516.9−518.1[d]	A $^2\Pi_u$−X $^2\Pi_g$	R_1, R_2; (1, 0, 0)−(0, 0, 0)
			BO_2	519.6−520.7[d]	A $^2\Pi_u$−X $^2\Pi_g$	R_1, R_2; (0, 2, 0)−(0, 0, 0)
w	549.4	547.8	BO_2	545.7−547.1[d]	A $^2\Pi_u$−X $^2\Pi_g$	R_1, R_2; (0, 0, 0)−(0, 0, 0)
			BO	551.3[b]	A $^2\Pi$−X $^2\Sigma^+$	(0, 3)
x	581.1 ± 1.4	579.4	BO_2	579.1−581.3	A $^2\Pi_u$−X $^2\Pi_g$	R_1, R_2; (0, 0, 0)−(1, 0, 0)
y	589.0	589.4	Na	589.00[c]	$2p^63s\ ^2S$ -$2p^63p\ ^2Po$	
	592.4 ± 1.9	590.2	Na	589.59[c]	$2p^63s\ ^2S$ -$2p^63p\ ^2Po$	
z	598.0 ± 5.3	594.6	TiO	584.9−590.0[f]	B $^3\Pi_{0,1,2}$−$X^3\Delta_{1,2,3}$	R; (1, 0)
			TiO	590.6−595.3[f]	B $^3\Pi_{0,1,2}$−$X^3\Delta_{1,2,3}$	R; (2, 1)
			TiO	595.3−600.5[f]	B $^3\Pi_{0,1,2}$−$X^3\Delta_{1,2,3}$	R; (3, 2)
a	609.9	609.8	Li	610.4[c]	$1s^22p\ ^2P°$ -$1s^23d\ ^2D$	

https://doi.org/10.1021/acs.jpca.1c08335
J. Phys. Chem. A 2022, 126, 125−144

Table 2. continued

peak or band	peak wavelength or band center (nm)[a]	peak wavelength or band center (nm)[a] with Span80	molecule, atom, or radical	ref. wavelength (nm)	transition	branch; vibrational quantum numbers: (ν', ν'') or (ν_1',ν_2', ν_3')−(ν_1'',ν_2'',ν_3'')
b	619.1 ± 1.2	614.8 ± 4.5	TiO	616.0−621.7[f,g]	B $^3\Pi_{0,1,2}$−X$^3\Delta_{1,2,3}$	R; (0, 0)
			BO_2	617.2−620.2[d]	A $^2\Pi_u$−X $^2\Pi_g$	R_1, R_2; (0, 0, 0)−(2, 0, 0)
c	640.6 ± 3.0	644.7 ± 4.1	BO_2	637.7−639.6[d]	A $^2\Pi_u$−X $^2\Pi_g$	R_1, R_2; (0, 0, 0)−(0, 0, 2)
d	673.2	673.2	Al	669.6−669.9[c]	$3s^24s\ ^2S-3s^25p\ ^2P^o$	
			Li	670.8[c]	$1s^22s\ ^2S\ -1s^22p\ ^2P^o$	
e	675.1	676.9	TiO	671.9−678.4[h]	A $^3\Phi_{2,3,4}$−X$^3\Delta_{1,2,3}$	R; (2, 1)
	678.9 ± 2.2	678.0				
f	715.2	712.4	TiO	705.6−712.8[h]	A $^3\Phi_{2,3,4}$−X$^3\Delta_{1,2,3}$	R; (0, 0)
			TiO	712.8−720.0[h]	A $^3\Phi_{2,3,4}$−X$^3\Delta_{1,2,3}$	R; (1, 1)
g		767.3	K	766.4 [9]	$3p^64s\ ^2S_{1/2}-3p^64p^2P^o_{3/2}$	
h	771.8	771.5	TiO	766.8−775.2[i]	A $^3\Phi_{2,3,4}$−X$^3\Delta_{1,2,3}$	R; (1, 2)
			K	769.9 [9]	$3p^64s\ ^2S_{1/2}-3p^64p^2P^o2_{3/2}$	
i		777.7 ± 1.2	TiO	774.5−783.0[i]	A $^3\Phi_{2,3,4}$−X$^3\Delta_{1,2,3}$	R; (2, 3)
j	783.4		Al	783.5−783.6[c]	$3s^23d\ ^2D-3s^26f\ ^2F^o$	
k	813.2	812.2	Li	812.6[c]	$1s^22p\ ^2Po-1s^23s^2S$	
l		818.1	Na	818.3−819.5 [9]	$2p^63p\ ^2P^o-2p^63d\ ^2D$	
m		840 ± 2	H_2O	≈811−839[d]	ro-vib. mode	(2, 1, 1)−(0, 0, 0)
n		925	H_2O	≈928−966[d]	ro-vib. mode	(2, 0, 1)−(0, 0, 0)
o		947	H_2O	≈928−966[d]	ro-vib. mode	(2, 0, 1)−(0, 0, 0)
p		995	H_2O			

[a]Measurements are accurate to within 1 nm unless stated otherwise. [b]Reference 119. [c]Reference 118. [d]Reference 126. [e]Reference 120. [f]Reference 122. [g]Reference 123. [h]Reference 124. [i]Reference 125. [j]Reference 57.

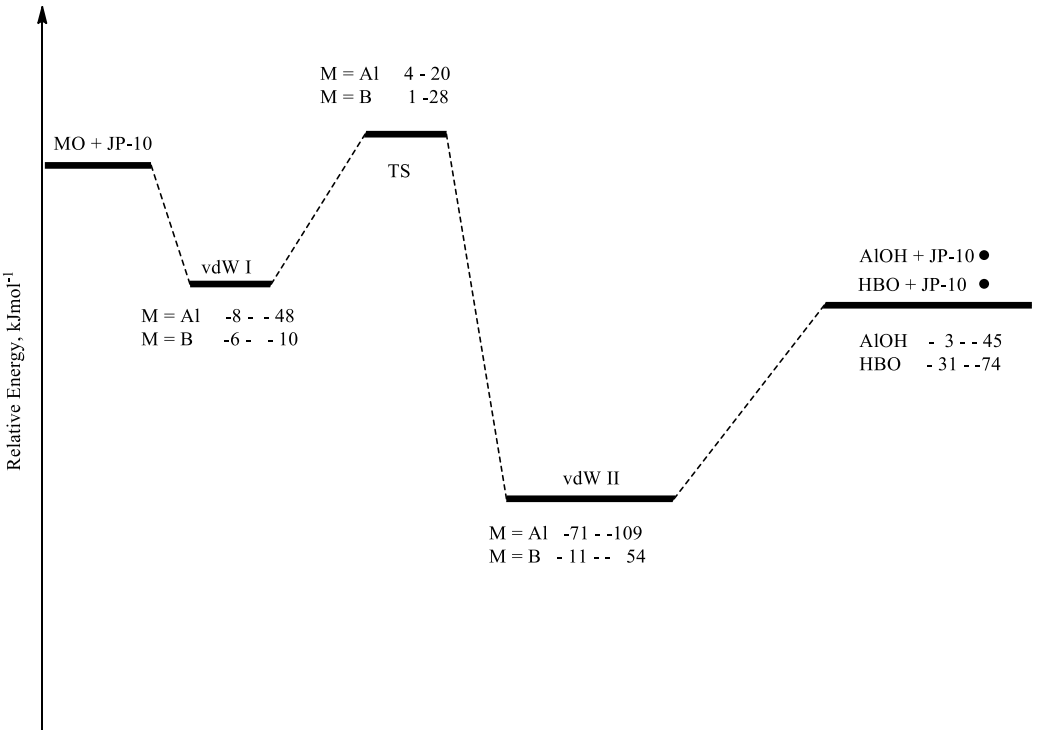

Figure 10. Schematic PES for the gas-phase reactions of BO and AlO with JP-10 leading to hydrogen abstraction products (AlOH and HBO) and JP-10 radicals R1−R6 (Figure 2).

2.5 mm at the 60 mm lens inside the recipient, should be unfocussed; in other words, the 532 nm laser beam has to pass through the 3 mm hole of the lens. Passing the laser beam through a lens without a hole results in a 45−50 μm laser spot size onto the droplet. This leads to the photochemical activation of JP-10 by the Ti−Al−B NPs. This photochemical processing results in five new Raman peaks: υ_{L1} to υ_{L5} (Figure S11). The low-frequency modes at 293 cm^{-1} (ν_{L1}) and 420 cm^{-1} (ν_{L2}) could be attributed to the prominent Ti−C and AL-C stretching modes observed in the literature for titanium carbides at, for example, 425 cm^{-1}. The higher-frequency modes at 1,838 cm^{-1} (ν_{L3}), 1,977 cm^{-1} (ν_{L4}), and 2,127 cm^{-1} (ν_{L5}) are likely linked to Al−H (ν_{L3}, ν_{L4}) and B−H stretching modes (ν_{L5}). Ti−H stretching modes are expected to arise in the range of 1400−

https://doi.org/10.1021/acs.jpca.1c08335
J. Phys. Chem. A 2022, 126, 125−144

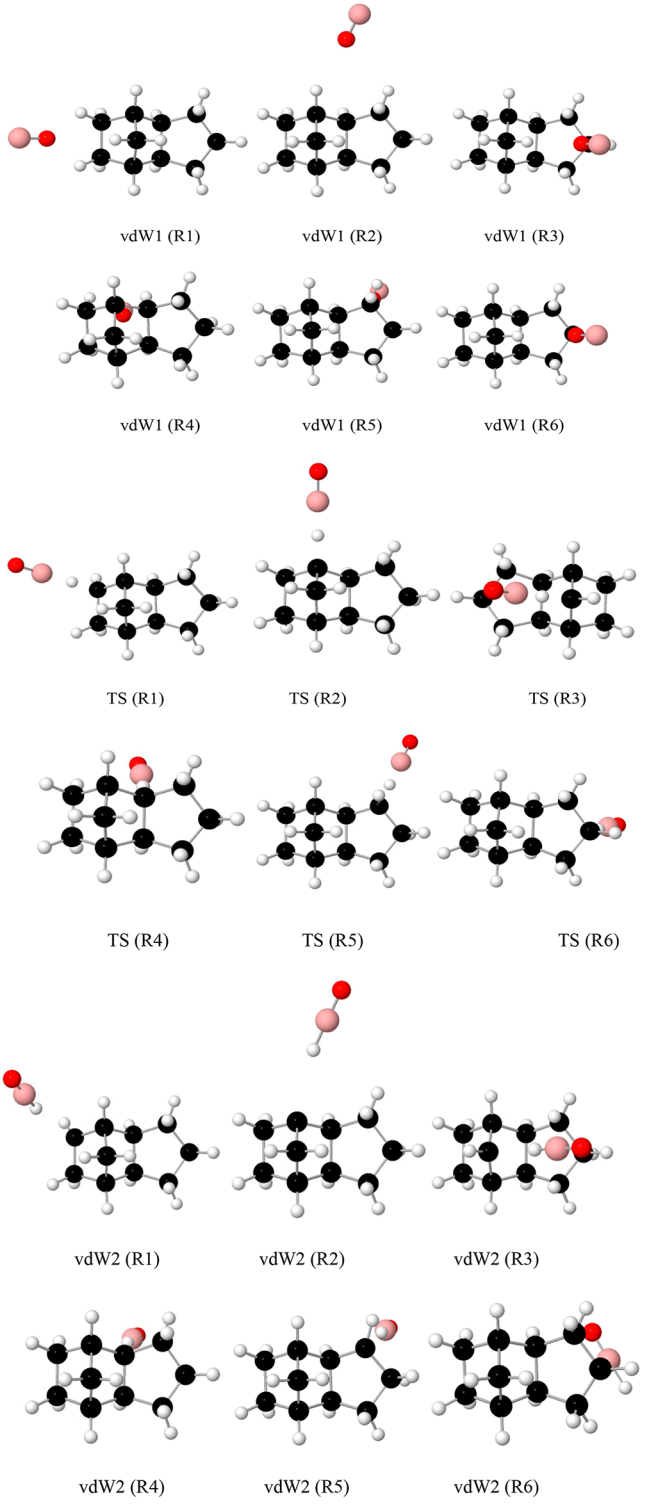

Figure 11. Structures of the vdW complexes and transition states for the hydrogen abstraction reactions of BO. The Cartesian coordinates and vibrational modes of these stationary points are compiled in Table S6. Atoms are color-coded in black (carbon), white (hydrogen), and orange (boron).

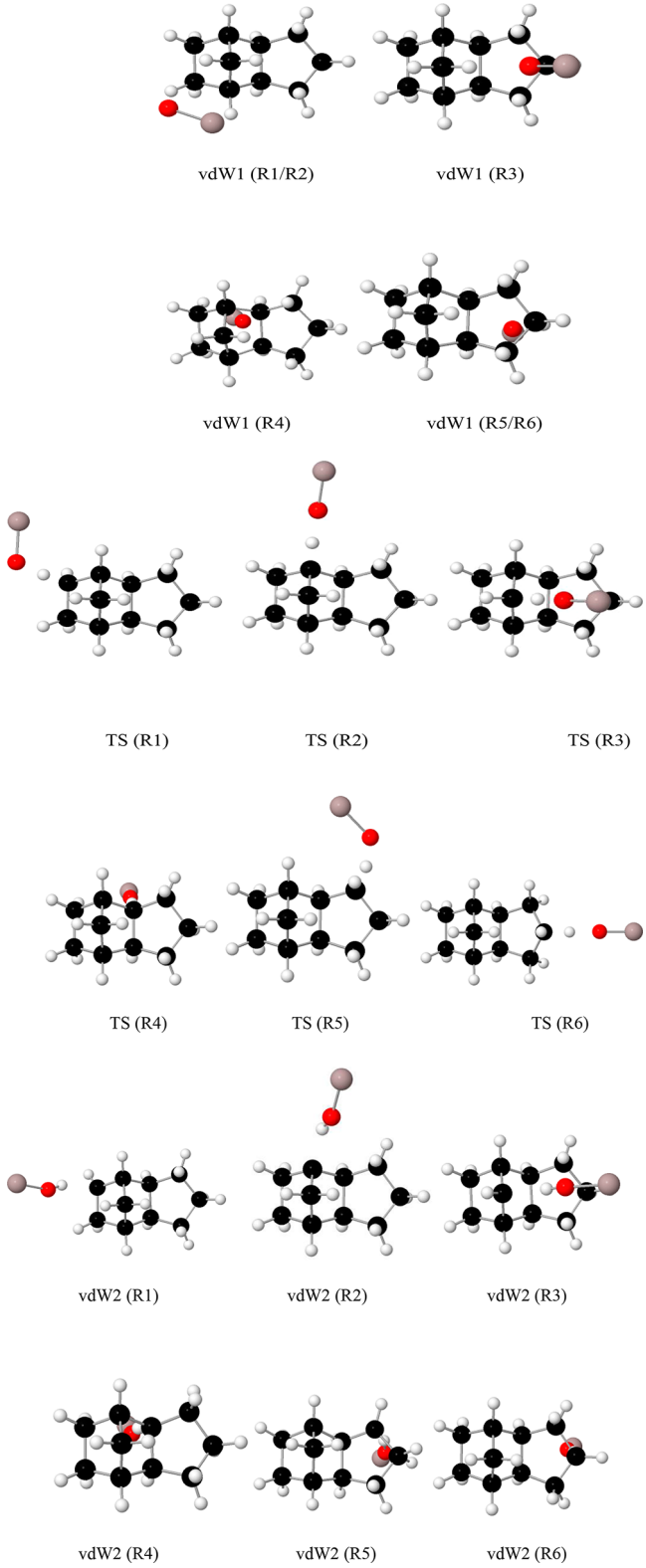

Figure 12. Structures of the vdW complexes and transition states for the hydrogen abstraction reactions of AlO. The Cartesian coordinates and vibrational modes of these stationary points are compiled in Table S6. Atoms are color-coded in black (carbon), white (hydrogen), and pink (aluminum).

1600 cm^{-1} but could not be assigned unambiguously. Nevertheless, these new features formed upon exposing Ti−Al−B NP-doped JP-10 to focused 532 nm light reveal an active photochemistry at 532 nm.[107−117]

4.2. Temperature Profiles. Figures 3−6 display the temperature profiles for the ignition of JP-10 droplets in the presence of (a) 2 wt % Ti−Al−B RMNPs (hereafter, Ti−Al−B

https://doi.org/10.1021/acs.jpca.1c08335
J. Phys. Chem. A 2022, 126, 125−144

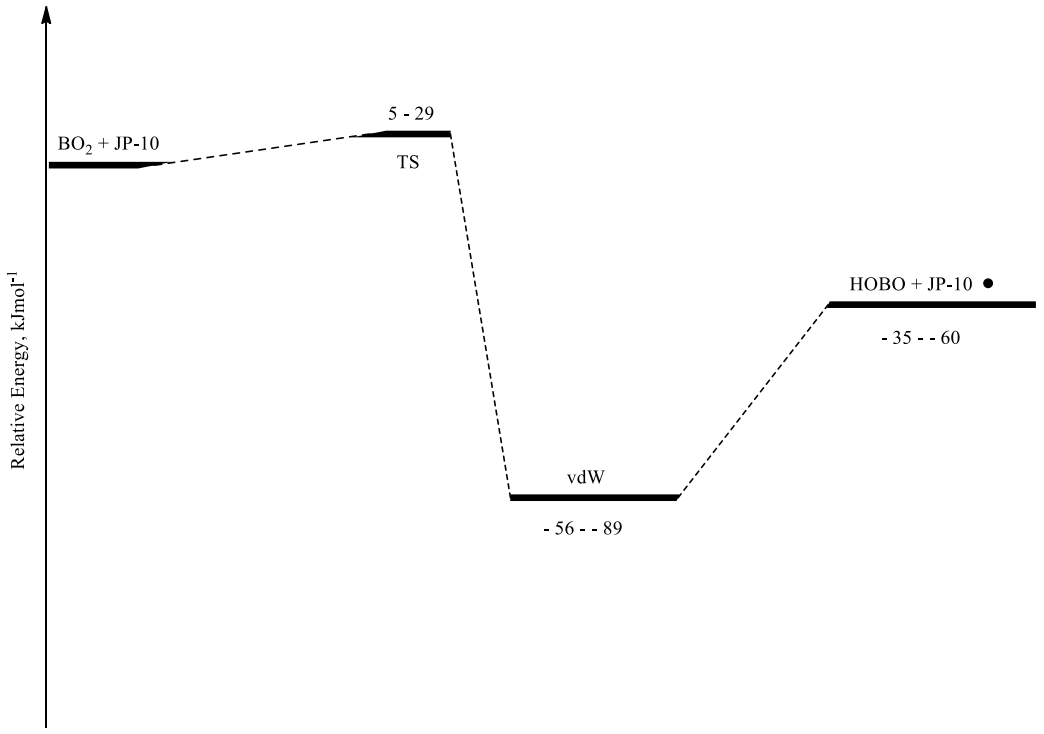

Figure 13. Top: Schematic PES for the gas-phase reactions of boron dioxide with JP-10 leading to hydrogen abstraction products (HOBO) and JP-10 radicals R1−R6 (Figure 2).

RMNPs), (b) 2 wt % Ti−Al−B RMNPs−1 wt % surfactant (hereafter, Ti−Al−B RMNPs−surfactant), (c) 2 wt % Al NPs (hereafter, Al NPs), and (d) 2 wt % Al NPs—1 wt % surfactant (hereafter, Al NPs−surfactant). The complete combustion process of droplets takes typically 100−150 ms. However, after about 40 ms, the system becomes unstable due to mass loss, and the droplet falls out of the trap since the resonance conditions are not met. These profiles reveal interesting findings. First, the temperature temporal profiles produced by igniting a JP-10 droplet containing 200 nm diameter Al particles (sample d) or 160 nm diameter Ti−Al−B particles (sample b) are compared (Figure 3). To help ensure that we investigated the effects of the different chemical compositions of samples (b,d) rather than how these particles were homogenized throughout JP-10, both types of particle were coated in the surfactant. No statistically significant differences in the ignition delay time, Δt, or the maximum rate of temperature increase, dT/dt_{max} were observed, that is, Δt (Ti−Al−B RMNPs−surfactant) = 0.8 ± 0.2 ms, Δt (Al NPs−surfactant) = 0.6 ± 0.2 ms, dT/dt_{max} (Ti−Al−B RMNPs−surfactant) = (2.5 ± 0.3) × 10^5 Ks^{-1}, and dT/dt_{max} (Al NPs−surfactant) = (2.3 ± 0.3) × 10^5 Ks^{-1}, where Δt is defined as the time to reach the ignition temperature of JP-10 at 509 K. However, the maximum flame temperature, T_m, which was attained after typically 20 to 35 ms, was likely lower for the Ti−Al−B particles, that is, T_m (Al NPs−surfactant) = 2870 ± 280 K versus T_m (Ti−Al−B RMNPs−surfactant) = 2550 ± 280 K. Furthermore, the probability of igniting the Al NPs was higher than for the Ti−Al−B RMNPs since the ignition percentages were 100 and 64%, respectively. This could be due to the higher barrier of oxidation of the RMNPs than that of the Al NPs.[54]

Second, to investigate the effects of the surfactant on the ignition delay time and the maximum flame temperature, in Figures 4−6, we compared the temperature temporal profiles produced by igniting a JP-10 droplet containing Ti−Al−B RMNPs and Al-NPs with and without the surfactant. The surfactant significantly reduced the ignition delay time from 10 ms to less than 0.5 ms, although it did not significantly affect the rate of temperature increase. The surfactant reduced the ignition delay time by helping the particles disperse uniformly throughout JP-10, which increases the probability that a particle will enter the path of the laser beam and, hence, be ignited (Section 4.3). As expected from the small amount of surfactant molecules in the solution, the maximum flame temperatures are identical within the experimental errors: T_m (Ti−Al−B RMNPs−surfactant) = 2550 ± 280 K versus T_m (Ti−Al−B RMNPs) = 2410 ± 340 K. Furthermore, the surfactant increased the probability of ignition from approximately 37 to 64%. To compare the maximum temperatures, T_{max}, reached with an improved statistical accuracy, the mean and standard deviation of T_{max} are quoted above for ten ignitions. However, to demonstrate the stochastic nature of the combustion process, the temperature temporal profiles in Figures 3−6 are presented for single ignitions only rather than as smeared-out averages over several ignitions. Thus, some of the variations in the shapes of the profiles that are apparent after about 15 ms are a consequence of the stochastic behavior of the flames within the FOV of the IR camera. The temperature temporal profiles produced by igniting a JP-10 droplet containing 200 nm diameter Al particles without (c) or with (d) the surfactant are presented in Figure 6. As for the Ti−Al−B particles, the surfactant reduced the ignition delay time from 1.5 ms to less than 0.5 ms and possibly increased the maximum flame temperature T_m (Al NPs−surfactant) = 2870 ± 280 K versus T_m (Al NPs) = 2710 ± 180 K. The reduction in Δt is less for the Al NPs than that for the Ti−Al−B RMNPs since the Al NPs were already well-dispersed throughout JP-10 before the addition of the surfactant. After reaching the maximum

https://doi.org/10.1021/acs.jpca.1c08335
J. Phys. Chem. A 2022, 126, 125−144

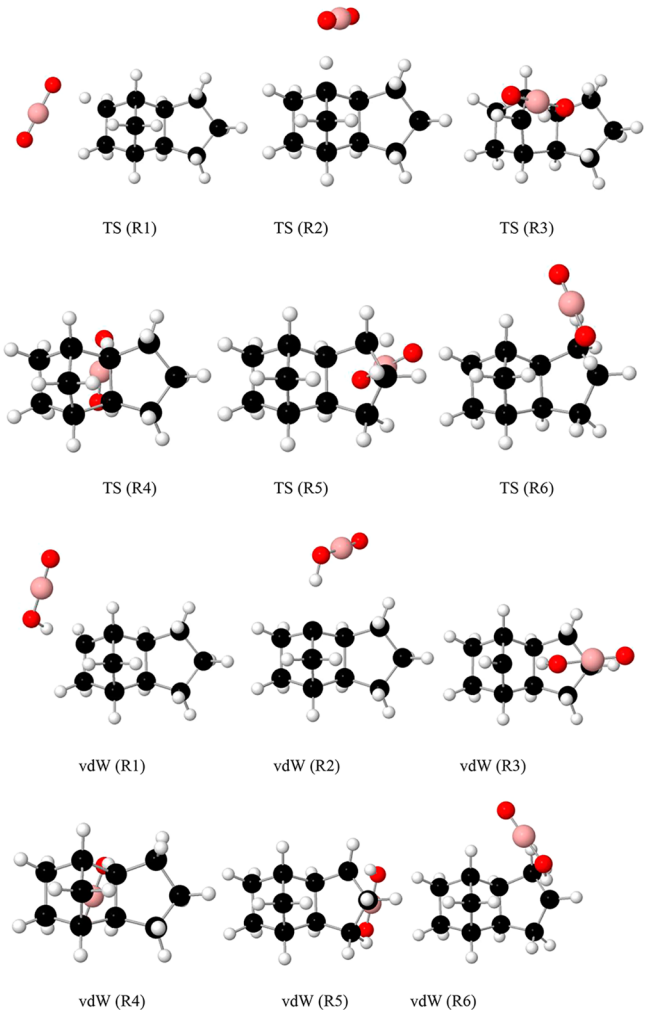

Figure 14. Structures of vdW complexes and transition states for the hydrogen abstraction pathways by boron dioxide. The Cartesian coordinates and vibrational modes of these stationary points are compiled in Table S6. Atoms are color-coded in black (carbon), white (hydrogen), and orange (boron).

temperature T_{max}, the temperatures decreased as the fuel was consumed.

4.3. Optical Ignition Videos. A visualization of the combustion process is displayed in Figure 7 for two JP-10 Ti−Al−B RMNPs−surfactant droplets. Once the CO_2 laser strikes the liquid droplet (t = 0 ms), part of the droplet vaporizes; this phase of evaporation is evident from the vapor cloud. During this phase, some of the nanoparticles also ignited, as shown through the orange-colored sparks ejected from the droplets while the vapor expanded. At this stage, JP-10 has not ignited yet. However, the burning nanoparticles ignited the JP-10 vapor as well, leading to the oxidation of the JP-10 fumes. This process is also visualized in Movies M1 and M2 (Supporting Information).

4.4. UV−Vis Emission Spectroscopy. The UV−vis emission spectra produced during the ignition of a JP-10 droplet containing Ti−Al−B RMNPs without or with the surfactant are shown in Figures 8 and 9, respectively. The features in the UV−vis emission spectra allow the atoms, molecules, and radicals formed by the oxidation of JP-10 and the Ti−Al−B RMNPs to be identified in addition to the impurities introduced in the manufacture of the particles.

Initially, we discuss the spectrum collected without the surfactant (Figure 8). First, the main group I alkali metal impurities lithium (Li), sodium (Na), and potassium (K) were detected (Table 2),[118] which produced the largest peaks in the spectrum by far. Li originated from the lithium aluminum hydride ($LiAlH_4$) used to prepare the Ti−Al−B RMNPs. Second, emissions were detected from radicals known to dominate the UV−vis spectra of hydrocarbon flames. The hydroxyl radical (OH) was assigned via four $A^2\Sigma^+-X^2\Pi$ transitions, which are distinguished by the different vibrational quantum numbers of the lower state, ν', and upper state, ν. Dicarbon (C_2) was identified by observing seven transitions of the Swan system, $d^3\Pi_g-a^3\Pi_u$.[39,40,119,120] The formyl radical (HCO) could only be assigned tentatively via a single emission line at 358.8 nm (Table 2).[119] Third, the data suggest that metal atoms evaporated from the Ti−Al−B RMNPs. Atomic aluminum could be detected through four transitions at 309.3, 394.4−396.2, 669.6−669.9, and 783.5−783.6 nm, whereas titanium was identified via four emission lines at 363.5−365.3, 375, 394.9−395.8, and 398.2−399.9 nm. In contrast, boron atoms were not detected. Considering the trend in the boiling points of pure aluminum, titanium, and boron of 2743, 3560, and 4893 K, respectively, our spectra suggest that the flame temperature was sufficient to evaporate aluminum and titanium from the RMNPs but not boron. The maximum flame temperature T_{max} of 2550 ± 280 K (section 4.2) is consistent with the absence of emissions from gas-phase boron. T_{max} is also below the boiling points of aluminum and titanium though, which appears to contradict the observation of emissions from gas-phase Al and Ti atoms. However, the ignition temperature of Al particles is known to decrease with diameter, for example, from 2350 K for a diameter of 100 μm to 933 K for a diameter of 100 nm. A similar trend is expected for Ti. The aforementioned trends in the boiling points provide a qualitative rationale for the detection of gas-phase aluminum and titanium but the absence of boron. Fourth, the emission spectra reveal the presence of rovibrationally excited metal monoxides, namely, aluminum monoxide (AlO), boron monoxide (BO), and titanium monoxide (TiO) via five, nine, and five emissions, respectively. The emissions of aluminum monoxide, which were also detected in the oxidation of JP-10 droplets doped with Al NPs,[65−68] originate from the $\Delta\nu$ = 2, 1, and 0 transitions of AlO ($A^2\Sigma^+-X^2\Sigma^+$), where $\Delta\nu$ denotes the change in the vibrational quantum number ν.[119] Titanium monoxide produces a series of broad emissions, the largest of which have maxima at around 595, 623, 675, 713, and 777 nm. The lower two emissions are produced by $B^3\Pi_{0,1,2}-X^3\Delta_{1,2,3}$ transitions, whereas the highest three emissions are due to $A^3\Phi_{2,3,4}-X^3\Delta_{1,2,3}$ transitions. The emissions near 595, 675, and 772 nm are partially hidden by the relatively much larger Na, Li, and K emission lines, respectively, although the 623 nm and 713 nm emissions appear as separate, broad bands with relatively small amplitudes.[121−124] Rovibrationally excited BO can be distinguished by several emissions from the BO α-system, the $A^2\Pi-X^2\Sigma^+$ system. Finally, the boron dioxide (BO_2) fluctuation bands are produced by the $A^2\Pi_u-X^2\Pi_g$ transitions and consist of waves showing maxima at 418, 453, 471, 490, 498, 519, 549, 581, 598, 610, and 640 nm. The BO_2 emissions are significantly larger than the BO bands and consequently partly mask them. The rapid oxidation of BO to boron dioxide has been established in molecular beam studies.[125] Similarly, the AlO emissions centered at 453, 471, and 490 nm overlap closely with the relatively much larger boron dioxide fluctuation emissions and, hence, do not appear as

https://doi.org/10.1021/acs.jpca.1c08335
J. Phys. Chem. A 2022, 126, 125−144

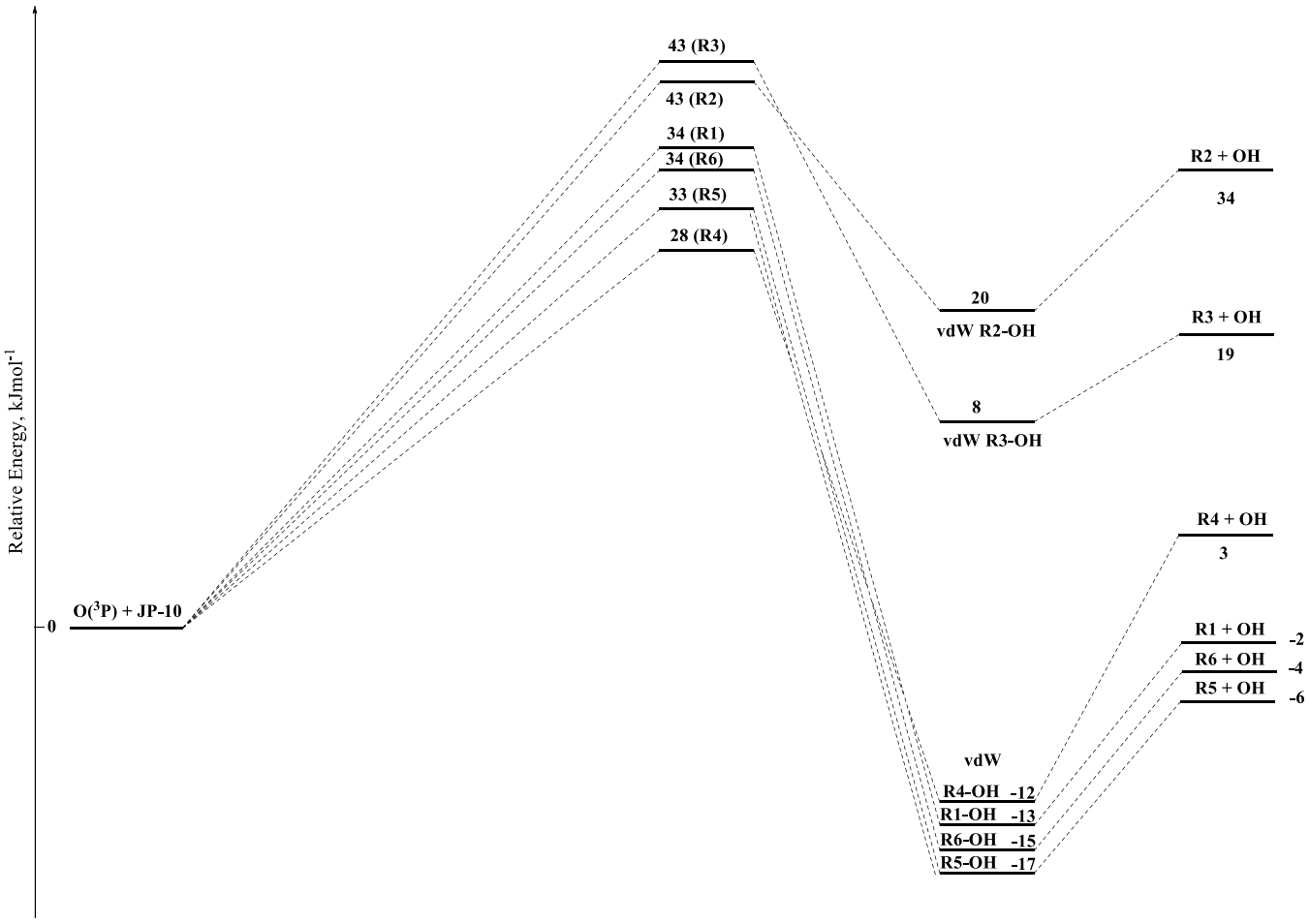

Figure 15. Schematic PES for the gas-phase reaction of ground-state oxygen atoms with JP-10 leading to the hydroxyl radical (OH) and JP-10 radicals R1−R6 calculated with CCSD/cc-pVTZ//B3LYP/cc-pVTZ (Figure 2).

separate, distinct features. No higher oxides of aluminum, titanium, or boron were observed.

The UV−vis emission spectrum produced during the ignition of a JP-10 droplet containing Ti−Al−B nanoparticles coated with the surfactant is shown in Figure 9a. The spectra with and without the surfactant differ in several respects. First, since the ignition occurred when a less amount of JP-10 had evaporated, the emission features appeared superimposed on a gray body background. Fitting a gray body spectrum enabled the flame temperature to be determined as 2600 ± 40 K, which is consistent with the mean value of 2710 ± 180 K obtained from the IR camera (Section 4.2). In Figure 9b,c, the same data are displayed except the gray body background has been subtracted to illustrate the emission structure more clearly. In some spectral regions of the fits, broad underlying peaks were included to account for variations in the background or unresolved bands, but these are not assigned in Figure 9 or included in Table 2. The increased statistical inaccuracy introduced by the gray body background obscured peaks (e−j, m, n, and p) produced by BO, BO_2, K, Ti, and HCO, which, in contrast, are clearly evident in Figure 8 without the surfactant. However, possibly because of the larger volume of combusting hydrocarbons available, an emission line appeared at 430 nm, produced by the $A^2\Delta-X\ ^2\Pi$ transition of the methylidyne radical (CH). The relative intensities of emissions from the alkali metals also differed with the surfactant; for example, the K line at around 770 nm is smaller, whereas the Na line at 770 nm is larger. Broad bands between approximately 800 and 1000 nm appeared with the surfactant, which are due to the emissions or absorptions from highly excited vibrational states of water molecules. The broad absorption region from approximately 900 to 1000 nm could be because of the water vapor produced in the combustion or absorption by the optical fiber.

4.5. FTIR Spectroscopy. Similar to the FTIR transmission spectra obtained for the oxidation of Al NP-doped JP-10,[65−68] the FTIR data collected after the combustion of the droplet revealed the gaseous products of the oxidation to be solely carbon dioxide (CO_2) and water (H_2O). These cover the asymmetric stretching mode [$\nu_{as}(H_2O)$] (3756 cm^{-1}) along with the bending mode [δ(OH)] (1600 cm^{-1}) of water. Carbon dioxide was identified via two combination bands [$1(\sigma_g^+)$ $+3(\sigma_u^+)$ and $1(\sigma_g^+)$ $+3(\sigma_u^+)$] at 3714 and 3612 cm^{-1}, respectively. Further absorptions were detected for the asymmetric stretching (σ_u^+) (2347, 2359, and 2279 cm^{-1}) and bending modes (π_u) (668, 648, 619, 655, 680, and 720 cm^{-1}) modes.

4.6. Computational Results. *4.6.1. Gas-Phase Reaction of Atoms with JP-10.* The detection of aluminum (Al, ^{2}P) and titanium atoms (Ti, ^{3}F) in the emission spectra necessitates an investigation of their reactivity with JP-10 molecules in the gas phase (Table S2). Although atomic boron was not observed, the calculations were expanded to the boron (B, ^{2}P)−JP-10 system for completeness. The reactions of Al(^{2}P), B(^{2}P), and Ti(^{3}F) with JP-10 lead via hydrogen abstraction to six chemically

https://doi.org/10.1021/acs.jpca.1c08335
J. Phys. Chem. A 2022, 126, 125−144

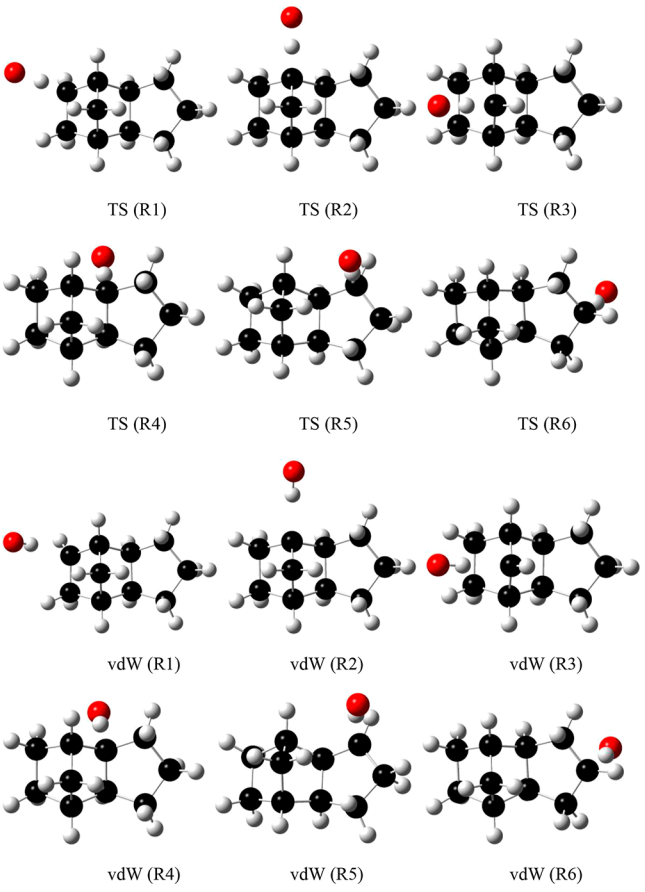

Figure 16. Rows 1 and 2: from left to right: structures of the transition states leading eventually to R1 and R6. Rows 3 and 4: from left to right: structures of vdW complexes leading eventually to R1 and R6. The Cartesian coordinates and vibrational modes of these stationary points are compiled in Table S7. Atoms are color-coded in black (carbon), white (hydrogen), and red (oxygen).

distinct JP-10 radicals (R1−R6) (Figure 2) in the overall endoergic reactions of 77−120, 129−173, and 217−262 kJ mol^{-1} for the aluminum, boron, and titanium systems, respectively. This correlates with the weaker metal−hydrogen single bond compared to the cleaved carbon−hydrogen bond. Overall, the strong endoergic nature of these reactions makes these reactions unfavorable.

4.6.2. Gas-Phase Reaction of Oxides with JP-10. The detection of AlO, BO, and TiO in the emission spectra motivated a computational exploration of the reactivity of these monoxides with JP-10 molecules in the gas phase. Since the overall hydrogen abstractions by TiO are highly endoergic by 209 (R1 + TiOH), 248 (R2 + TiOH), 231 (R3 + TiOH), 214 (R4 + TiOH), 204 (R5 + TiOH), and 205 kJ mol^{-1} (R6 + TiOH), these reactions are not competitive with the hydrogen abstractions by AlO and BO, as detailed below. Consequently, complete potential energy surfaces (PESs) are only computed for the abstraction of hydrogen from JP-10 by AlO and BO (Table S3 and Figures 10−12). In each system, the metal monoxide and JP-10 yield vdW complexes in the entrance channel (vdW I). The formation of these vdW complexes is governed by attractive, long-range dipole (metal monoxide)−dipole (JP-10) interactions. Once again, since JP-10 holds six nonequivalent hydrogen atoms, six chemically nonequivalent vdW complexes exist in the entrance channel.

Considering the AlO-JP-10 system (Figures 10−12 and Table S3), the vdW complexes at sites 3−6 are weakly stabilized by 8−48 kJ mol^{-1} with respect to the separated reactants. At all six sites, the reactants were found to isomerize via hydrogen abstraction to a vdW complex of aluminum monohydroxide (AlOH) plus the JP-10 radical (vdW II). It is important to note that the hydrogen abstraction processes involve an abstraction of the hydrogen with the oxygen atom of the aluminum monoxide radical; further, the transition states are located above the energy of the separated reactants by 4−20 kJ mol^{-1}. The resulting vdW II complexes reside in potential energy wells of 71−109 kJ mol^{-1} with respect to the separated reactants and may undergo unimolecular decomposition to the JP-10 radicals (R1−R6) and aluminum monohydroxide (AlOH) in overall exoergic reactions, releasing 4−45 kJmol^{-1}.

With respect to the BO-JP-10 system (Figures 10−12 and Table S3), the vdW complexes are stabilized by 6−10 kJ mol^{-1} with respect to the separated reactants and isomerize via hydrogen abstraction to a vdW complex of boron hydride oxide (HBO) plus the JP-10 radical (vdW II). Considering the stronger H−B bond versus the Al−H bond, it is important to rationalize that the BO radical abstracts the hydrogen from JP-10 with the boron atom, but aluminum monoxide abstracts atomic hydrogen with the oxygen atom. The transition states are located above the energy of the separated reactants by 1−28 kJ mol^{-1}. The vdW II complexes are stabilized by 11−54 kJmol^{-1} with respect to the separated reactants and fragment via unimolecular decomposition to the JP-10 radicals (R1−R6) and boron hydride oxide (HBO) in overall exoergic reactions (−31 to −74 kJ mol^{-1}).

4.6.3. Gas-Phase Reaction of Dioxides with JP-10. Boron dioxide (BO_2, $X^2\Sigma_g^+$) represents the only dioxide detected via UV−vis spectroscopy; neither aluminum dioxide (AlO_2, $X^2\Sigma_g^+$) nor titanium dioxide (TiO_2, X^1A_1) was observable in emission. The abstraction pathways of BO_2 do not involve the formation of initial vdW complexes but proceed directly from the reactants via six distinct transition states located between 5 and 29 kJ mol^{-1} above the separated reactants (Figures 13 and 14 and Table S4). These transition states connect the reactants with a vdW complex in the exit channel of meta boric acid (HOBO) and six distinct JP-10 radicals (R1−R6). These complexes are stabilized by 56−90 kJ mol^{-1} with respect to the separated reactants and undergo unimolecular decomposition to the JP-10 radicals (R1−R6) and HOBO in overall exoergic reactions (−35 to −60 kJ mol^{-1}).

4.6.4. Gas-Phase Reaction of O(^{3}P) with JP-10. As an atomic oxidizer, the PESs of ground-state oxygen atoms with JP-10 are more diverse than those of the AlO− and BO−JP-10 surfaces, as detailed in Figures 15 and 16 and Tables S5 and S7. Essentially, O(^{3}P) can abstract atomic hydrogen from one of the six chemically nonequivalent C−H bonds of JP-10. However, these abstraction routes are not initiated by the formation of vdW complexes between atomic oxygen and JP-10 in the entrance channel but proceed from the reactants via six distinct transition states located between 28 and 43 kJ mol^{-1} above the separated reactants. Prior to the formation of the separated products, all pathways involve vdW complexes in the exit channels, of which four are below (−12 to −17 kJ mol^{-1}; R1 and R4−R6) but two are above (+8 to + 20 kJ mol^{-1}; R2 and R3) the energies of the separated products. Correspondingly, our calculations suggest that three exit channels to R1, R5, and R6 plus the hydroxyl radical are weakly exoergic by −2, −6, and −4 kJmol^{-1}, respectively, whereas the three exit channels to R2, R3, and R4

https://doi.org/10.1021/acs.jpca.1c08335
J. Phys. Chem. A 2022, 126, 125−144

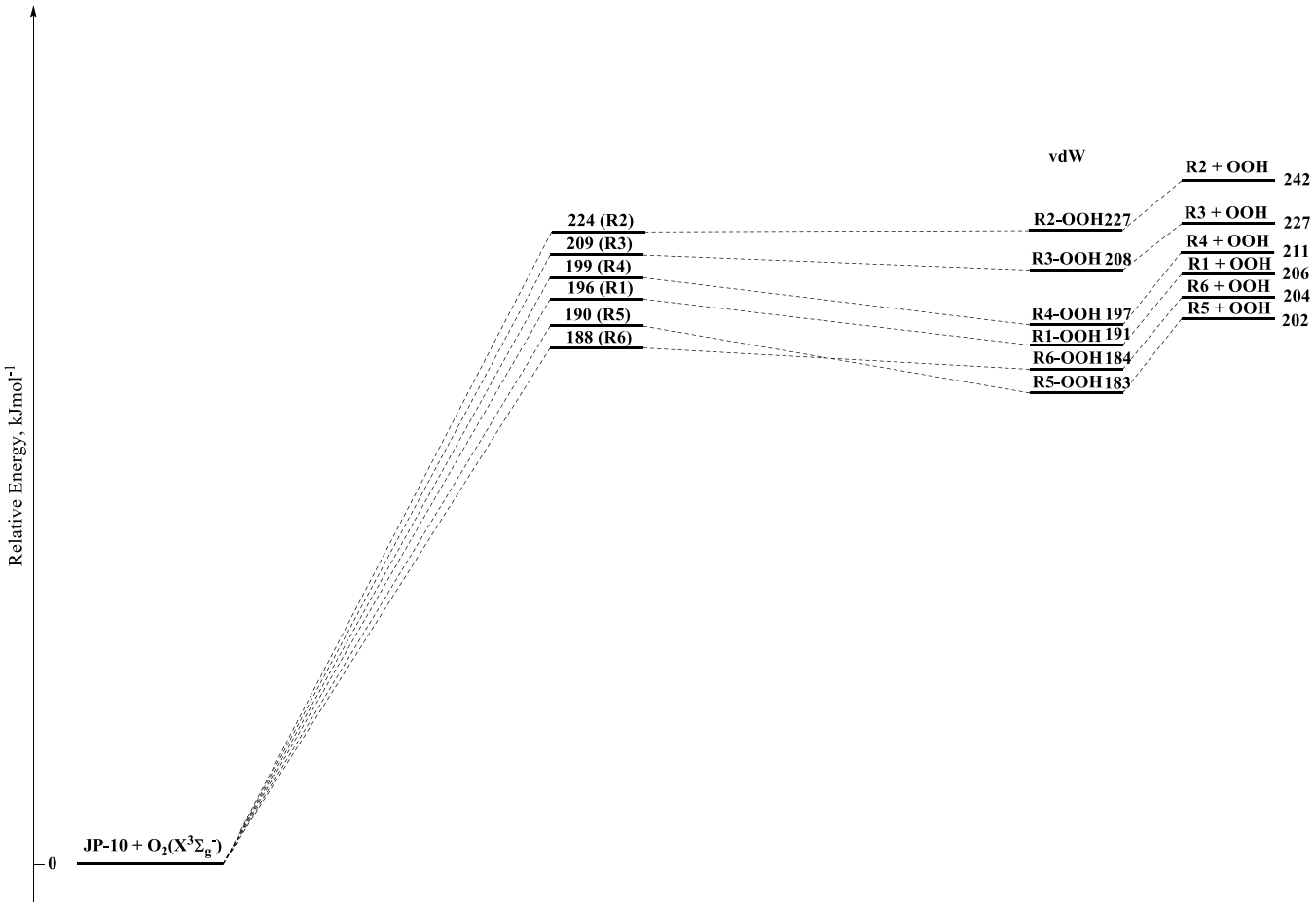

Figure 17. Schematic PES for the gas-phase reaction of ground-state molecular oxygen with JP-10 leading to the hydroxyperoxy radical (HO2) and JP-10 radicals R1−R6 calculated with CCSD/cc-pVTZ//B3LYP/cc-pVTZ; vdW-R2-O2H, −R4−O2H, and tsR4 are obtained at the CCSD/cc-pVTZ//MP2/cc-pVDZ level of theory.

plus hydroxyl are endoergic by 34, 19, and 3 kJ mol^{-1}, respectively. However, it shall be stressed that the formation of each of the R1−R6 radicals along with the hydroxyl radical has to pass a transition state, which is located above the energy of the separated reactants (Figures 10−12).

It should be highlighted that in the $O(^3P)$—JP-10 system, the lowest-energy transition state is located 28 kJ mol^{-1} above the separated reactants; in this pathway, atomic hydrogen is abstracted from the C4 position, leading effectively to a vdW complex between the hydroxyl radical and R4. For the BO, AlO, and BO_2 abstraction pathways, with the exception of the transition state connecting the reactants to the vdW complex between HOBO and the R6 radical, all transition states are lower than 29 $kJmol^{-1}$. Consequently, BO, AlO, and BO_2 are expected to abstract atomic hydrogen faster from the JP-10 reactant than that from $O(^3P)$.

4.6.5. Gas-Phase Reaction of $O_2(X^3\Sigma^-_g)$ with JP-10. Considering the weaker H−O bond in the hydroxyperoxy radical (HO_2, X^2A') compared to the C−H bond strengths in JP-10, the hydrogen abstraction pathways of molecular oxygen from JP-10 are overall highly endoergic between 202 and 242 kJ mol^{-1} (Figures 17 and 18 and Table S5). Similar to atomic oxygen, no vdW complexes could be located in the entrance channel, and the abstraction reaction may pass six distinct transition states located between 188 and 209 kJ mol^{-1} above the separated reactants. Prior to the formation of the separated reactants, the JP-10 radicals R1−R6 form six distinct vdW complexes with the hydroxyperoxy radical. These are located between 183 and 208 kJ mol^{-1} above the energies of the separated reactants before they are formed in the overall endoergic reactions (202−242 kJ mol^{-1}) to the JP-10 radicals (R1−R6) along with the hydroxyperoxy radical (HO_2, X^2A').

5. CONCLUSIONS

This work represents the first report on the combustion of the single levitated droplet of JP-10 doped with Ti−Al−B-based RMNPs in an oxygen (60%)−argon (40%) atmosphere utilizing an ultrasonic levitator. Droplets were ignited by a carbon dioxide laser, and the oxidation processes were observed by using FTIR and UV−vis spectroscopy along with infrared thermal imaging and high-speed optical cameras. This study resulted in interesting findings.

First, recall that under the same experimental conditions, pure JP-10 droplets did not ignite.[65−68] Monitored via the high-speed optical camera, the carbon dioxide laser led to the evaporation of the droplet prior to the autoignition temperature of JP-10 of 509 K. The addition of RMNPs could have increased the boiling point of JP-10. However, JP-10 droplets doped with silicon dioxide (SiO_2), titanium dioxide (TiO_2), aluminum oxide (Al_2O_3), and copper (II) oxide (CuO) nanoparticles of comparable size to the Ti−Al−B RMNPs did not ignite either.[65,66,68] Consequently, the RMNPs must have played an active role in the ignition of JP-10.

https://doi.org/10.1021/acs.jpca.1c08335
J. Phys. Chem. A 2022, 126, 125−144

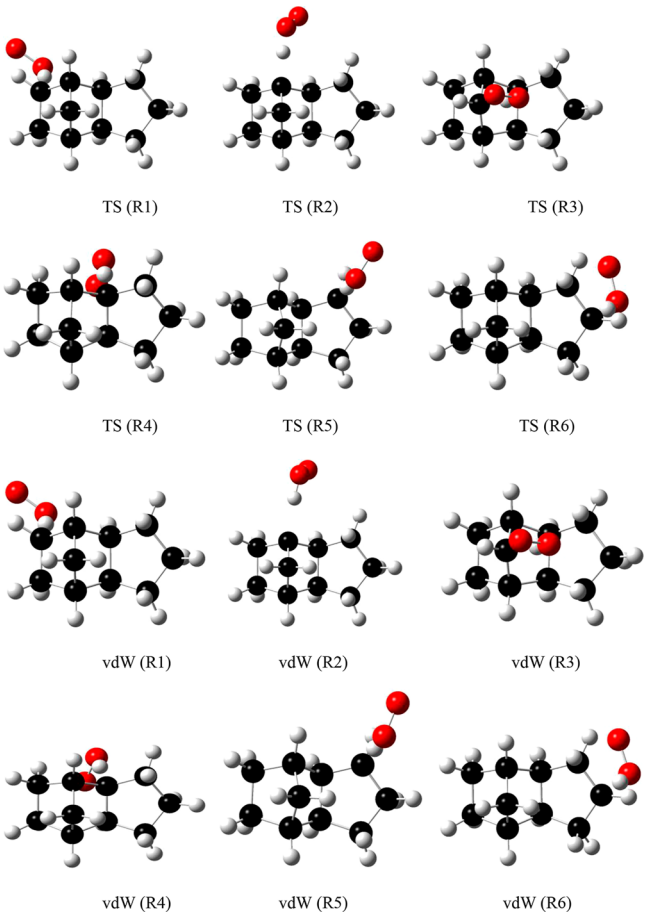

Figure 18. Rows 1 and 2: from left to right: structures of the transition states leading eventually to R1 and R6. Rows 3 and 4: from left to right: structures of vdW complexes leading eventually to R1 and R6. The Cartesian coordinates and vibrational modes of these stationary points are compiled in Table S7. Atoms are color-coded in black (carbon), white (hydrogen), and red (oxygen).

Second, the UV−vis emission spectra revealed the presence of gas-phase aluminum (Al) and titanium (Ti) atoms. Recalling the trends of boiling points of aluminum (2743 K), titanium (3560 K), and boron (4893 K), typical flame temperatures of 2550 ± 280 K, which are higher than the boiling point of aluminum and should lead to a sufficient vapor pressure of titanium to be detected spectroscopically, are sufficient to evaporate aluminum and titanium but not boron. These atoms can be oxidized in the gas phase by molecular oxygen to the UV−vis spectroscopically detected AlO and TiO intermediates in overall exoergic reactions of 14 and 170 kJ mol^{-1}, respectively.[126] These detected transient species rationalize the X-ray powder diffraction identification of the terminal end products of the oxidation of titanium dioxide (TiO_2) and aluminum oxide (Al_2O_3) in solid residues of RMNP-doped *n*-decane flames.[57] The analysis of the optical ignition videos also supports that the nanoparticles are ignited prior to the oxidation of JP-10, as evident from the orange-colored sparks emitted from the droplets while the vapor expanded. Considering the absence of gas-phase boron atoms, the detection of BO proposed active surface chemistry through the oxidation of the RMNPs and the release of at least BO into the gas phase. The oxidation of gas-phase BO by molecular oxygen to BO_2 plus atomic oxygen is exoergic by 76 kJ mol^{-1} and hence could operate in the gas phase, although an involvement of the surface oxidation processes of RMNPs to form BO_2 cannot be discounted. Note that emission lines from BO_2 were also observed in *n*-decane[57] and methane flames doped with RMNPs.[59] The elevated temperature of methane flames also resulted in emissions from AlO. Finally, the UV−vis emission spectra revealed the key reactive intermediates (OH, CH, C_2, and HCO) of the oxidation of JP-10.

Third, electronic structure calculations reveal that reactive radicals have a profound impact on the oxidation of JP-10. Although TiO can react to produce titanium dioxide (TiO_2) powders,[57] TiO does not engage in an active JP-10 chemistry as all of its abstraction pathways are highly endoergic by at least 209 kJ mol^{-1}. This is similar to atomic aluminum and boron, whose hydrogen abstraction reactions from JP-10 are endoergic by at least 77 and 129, respectively. Therefore, aluminum and titanium react preferentially with molecular oxygen to form their monoxides, as detected spectroscopically. The formation of gas-phase BO, AlO, and BO_2 supplies a highly reactive pool of radicals, which can abstract hydrogen from JP-10 via low-lying transition states ranging only 1 (BO), 4 (AlO), and 5 kJ mol^{-1} (BO_2) above the separated reactants, thereby forming JP-10 radicals R1−R6 (Figure 2) along with the hydrogen abstraction products HBO, AlOH, and HOBO in overall exoergic reactions. The hydrogen atoms are abstracted preferentially from the bridging methylene moiety (CH_2) or methylidyne functional group (CH), leading to R3 and R4, respectively. Importantly, these abstraction barriers are well below the barriers of abstractions for ground-state atomic oxygen and molecular oxygen, which exceed 28 and 188 kJ mol^{-1}, respectively. In this sense, gas-phase BO, AlO, and BO_2 catalyze the oxidation of gas-phase JP-10 via hydrogen abstraction, thereby forming highly reactive JP-10 radicals such as R3 and R4, which can then react barrierlessly via rapid radical atom/molecule reaction involving atomic and molecular oxygen and hence drive the oxidation of JP-10. Therefore, the addition of RMNPs to JP-10 not only provides a higher-energy-density fuel but is also expected to lead to shorter ignition delays than that of pure JP-10 owing to the highly reactive pool of BO, AlO, and BO_2 radicals formed in the initial stages of the oxidation process. These predicted reduced ignition delays were observed by Epshteyn et al. in RMNP-doped JP-5.[61] Overall, the studies presented here represent the first step toward a systematic understanding of the oxidation of JP-10 doped with RMNPs.

■ ASSOCIATED CONTENT

Supporting Information

The Supporting Information is available free of charge at https://pubs.acs.org/doi/10.1021/acs.jpca.1c08335.

Calibration curves used to calibrate the low-energy region of Raman data (100−2400 cm^{-1}) and high-energy region of Raman data (2200−4000 cm^{-1}); comparison between the calculated vibrational wavenumber and the experimental Raman wavenumber and the experimental FTIR wavenumber of the normal modes of *exo*-tetrahydrodicyclopentadiene; Raman spectra of pure JP-10, JP-10-Al, and JP-10-Ti−Al−B NPs (RMNPs); FTIR spectra of pure JP-10; Raman spectra of new peaks resulting from photochemically activated JP-10-Ti-Al-B NPs (RMNPs) by a tightly focused 532 nm laser beam (45−50 μm) at 1 kHz; vibrational mode assignments for the observed peaks in the Raman spectra of JP-10, JP-10-Al, and JP-10-Ti−Al−B NPs (RMNPs), Ti−Al−B NPs (RMNPs), and

https://doi.org/10.1021/acs.jpca.1c08335
J. Phys. Chem. A 2022, 126, 125−144

the FTIR Spectra of JP-10; total energies and zero-point energy-corrected total energies simulated for the transition states, reactive intermediates, complexes, and the products for the reactions of AlO, BO, and BO_2 with JP-10; Cartesian coordinates and vibrational frequencies of vdW complexes, transition states, and products of the reactions of BO, AlO, and BO_2 with JP-10; and Cartesian coordinates and vibrational frequencies of vdW complexes, transition states, and products of the reactions of atomic and molecular oxygen with JP-10 (PDF)

Optical high-speed videos of the ignition of a JP-10 droplet containing RMNPs and the surfactant (PPTX)

AUTHOR INFORMATION

Corresponding Authors

Ralf I. Kaiser − *Department of Chemistry, University of Hawaii at Manoa, Honolulu, Hawaii 96822, United States;* orcid.org/0000-0002-7233-7206; Email: ralfk@hawaii.edu

Mark Palenik − *U.S. Naval Research Laboratory, Washington, D.C., Washington, D.C. 20375, United States;* Email: mark.palenik@nrl.navy.mil

Albert Epshteyn − *U.S. Naval Research Laboratory, Washington, D.C., Washington, D.C. 20375, United States;* orcid.org/0000-0002-4489-2296; Email: albert.epshteyn@nrl.navy.mil

Agnes H. H. Chang − *Department of Chemistry, National Dong Hwa University, Hualien 974, Taiwan;* Email: hhchang@gms.ndhu.edu.tw

Authors

Stephen J. Brotton − *Department of Chemistry, University of Hawaii at Manoa, Honolulu, Hawaii 96822, United States*

Sahan D. Perera − *Department of Chemistry, University of Hawaii at Manoa, Honolulu, Hawaii 96822, United States;* orcid.org/0000-0002-4577-9025

Anupam Misra − *Department of Chemistry, University of Hawaii at Manoa, Honolulu, Hawaii 96822, United States*

N. Fabian Kleimeier − *Department of Chemistry, University of Hawaii at Manoa, Honolulu, Hawaii 96822, United States;* orcid.org/0000-0003-1767-897X

Andrew M. Turner − *Department of Chemistry, University of Hawaii at Manoa, Honolulu, Hawaii 96822, United States*

Matthew T. Finn − *U.S. Naval Research Laboratory, Washington, D.C., Washington, D.C. 20375, United States;* orcid.org/0000-0001-9474-7022

Bing-Jian Sun − *Department of Chemistry, National Dong Hwa University, Hualien 974, Taiwan*

Li-Jie Zhang − *Department of Chemistry, National Dong Hwa University, Hualien 974, Taiwan*

Complete contact information is available at: https://pubs.acs.org/10.1021/acs.jpca.1c08335

Notes

The authors declare no competing financial interest.

ACKNOWLEDGMENTS

The Hawaii group was supported by the Office of Naval Research (ONR) under contract number N000141912083. The work performed by NRL was supported by the ONR under contract numbers N0001421WX00908 and N0001419WX00827. B.J.S., L.J.Z., and A.H.H.C. appreciate the computer resources in computations provided by the National Center for High-performance Computer in Taiwan.

REFERENCES

(1) Chung, H. S.; Chen, C. S. H.; Kremer, R. A.; Boulton, J. R.; Burdette, G. W. Recent Developments in High-Energy Density Liquid Hydrocarbon Fuels. *Energy Fuels* **1999**, *13*, 641−649.

(2) Osmont, A.; Gökalp, I.; Catoire, L. Evaluating Missile Fuels. *Propellants, Explos., Pyrotech.* **2006**, *31*, 343−354.

(3) Zettervall, N. Reduced Chemical Kinetic Reaction Mechanism for JP-10-Air Combustion. *Energy Fuels* **2020**, *34*, 16624−16635.

(4) Wu, J.; Gao, L. G.; Ning, H.; Ren, W.; Truhlar, D. G. Direct Dynamics of a Large Complex Hydrocarbon Reaction System: The Reaction of Oh with Exo-Tricyclodecane (the Main Component of Jet Propellant-10). *Combust. Flame* **2020**, *216*, 82−91.

(5) Maurice, L. Q.; Lander, H.; Edwards, T.; Harrison, W. E., III Advanced Aviation Fuels: A Look Ahead Via a Historical Perspective. *Fuel* **2001**, *80*, 747−756.

(6) Van Devener, B.; Anderson, S. L. Breakdown and Combustion of JP-10 Fuel Catalyzed by Nanoparticulate CeO2 and Fe2O3. *Energy Fuels* **2006**, *20*, 1886−1894.

(7) Nakra, S.; Green, R. J.; Anderson, S. L. Thermal Decomposition of JP-10 Studied by Micro-Flowtube Pyrolysis-Mass Spectrometry. *Combust. Flame* **2006**, *144*, 662−674.

(8) Vandewiele, N. M.; Magoon, G. R.; Van Geem, K. M.; Reyniers, M.-F.; Green, W. H.; Marin, G. B. Experimental and Modeling Study on the Thermal Decomposition of Jet Propellant-10. *Energy Fuels* **2014**, *28*, 4976−4985.

(9) Herbinet, O.; Sirjean, B.; Bounaceur, R.; Fournet, R.; Battin-Leclerc, F.; Scacchi, G.; Marquaire, P.-M. Primary Mechanism of the Thermal Decomposition of Tricyclodecane. *J. Phys. Chem. A* **2006**, *110*, 11298−11314.

(10) Nageswara Rao, P.; Kunzru, D. Thermal Cracking of JP-10: Kinetics and Product Distribution. *J. Anal. Appl. Pyrolysis* **2006**, *76*, 154−160.

(11) Striebich, R. C.; Lawrence, J. Thermal Decomposition of High-Energy Density Materials at High Pressure and Temperature. *J. Anal. Appl. Pyrolysis* **2003**, *70*, 339−352.

(12) Wohlwend, K.; Maurice, L. Q.; Edwards, T.; Striebich, R. C.; Vangsness, M.; Hill, A. S. Thermal Stability of Energetic Hydrocarbon Fuels for Use in Combined Cycle Engines. *J. Propul. Power* **2001**, *17*, 1258−1262.

(13) Xing, Y.; Fang, W.; Xie, W.; Guo, Y.; Lin, R. Thermal Cracking of JP-10 under Pressure. *Ind. Eng. Chem. Res.* **2008**, *47*, 10034−10040.

(14) Li, G.; Zhang, C.; Wei, H.; Xie, H.; Guo, Y.; Fang, W. Investigations on the thermal decomposition of JP-10/ iso -octane binary mixtures. *Fuel* **2016**, *163*, 148−156.

(15) Bruno, T.; Bruno, T. J.; Huber, M.; Laesecke, A.; Lemmon, E. W.; Perkins, R. A. Thermochemical and Thermophysical Properties of JP-10. *Tech. Rep. NISTIR* **2006**, *6640*, 325.

(16) Park, S. H.; Kwon, C. H.; Kim, J.; Chun, B.-H.; Kang, J. W.; Han, J. S.; Jeong, B. H.; Kim, S. H. Thermal Stability and Isomerization Mechanism of Exo-Tetrahydrodicyclopentadiene: Experimental Study and Molecular Modeling. *Ind. Eng. Chem. Res.* **2010**, *49*, 8319−8324.

(17) Li, H.; Liu, G.; Jiang, R.; Wang, L.; Zhang, X. Experimental and Kinetic Modeling Study of Exo-Tcd Pyrolysis under Low Pressure. *Combust. Flame* **2015**, *162*, 2177−2190.

(18) Vandewiele, N. M.; Magoon, G. R.; Van Geem, K. M.; Reyniers, M.-F.; Green, W. H.; Marin, G. B. Kinetic Modeling of Jet Propellant-10 Pyrolysis. *Energy Fuels* **2015**, *29*, 413−427.

(19) Yue, L.; Xie, H.-J.; Qin, X.-M.; Lu, X.-X.; Fang, W.-J. A Dft Study on the Thermal Cracking of JP-10. *J. Mol. Model.* **2013**, *19*, 5355−5365.

(20) Chenoweth, K.; Van Duin, A. C. T.; Dasgupta, S.; Goddard III, W. A., Iii Initiation Mechanisms and Kinetics of Pyrolysis and Combustion of JP-10 Hydrocarbon Jet Fuel. *J. Phys. Chem. A* **2009**, *113*, 1740−1746.

(21) Magoon, G. R.; Aguilera-Iparraguirre, J.; Green, W. H.; Lutz, J. J.; Piecuch, P.; Wong, H.-W.; Oluwole, O. O. Detailed chemical kinetic modeling of JP-10 (exo-tetrahydrodicyclopentadiene) high-temper-

ature oxidation: Exploring the role of biradical species in initial decomposition steps. *Int. J. Chem. Kinet.* **2012**, *44*, 179−193.
(22) Hudzik, J. M.; Asatryan, R.; Bozzelli, J. W. Thermochemical Properties of exo-Tricyclo[5.2.1.02,6]decane (JP-10 Jet Fuel) and Derived Tricyclodecyl Radicals. *J. Phys. Chem. A* **2010**, *114*, 9545−9553.
(23) Hudzik, J. M.; Castillo, Á.; Bozzelli, J. W. Bond Energies and Thermochemical Properties of Ring-Opened Diradicals and Carbenes of exo-Tricyclo[5.2.1.02,6]decane. *J. Phys. Chem. A* **2015**, *119*, 9857−9878.
(24) Zehe, M. J.; Jaffe, R. L. Theoretical Calculation of Jet Fuel Thermochemistry. 1. Tetrahydrodicylopentadiene (JP10) Thermochemistry Using the CBS-QB3 and G3(MP2)//B3LYP Methods. *J. Org. Chem.* **2010**, *75*, 4387−4391.
(25) Cheng, S.-S.; Liou, K.-F.; Lin, Y.-T. High Energy Fuels I: A Novel Preparation of Exo-Tetrahydrodicyclopentadiene by Isomerization of Endo-Tetrahydrodicyclopentadiene. *J. Chin. Chem. Soc.* **1986**, *33*, 335−340.
(26) Prakash, O.; Tiwari, R.; Kalra, S. L.; Venkataramani, P. Isomerisation of Endo-Tetrahydrodicyclopentadiene to Exo-Tetrahydrodicyclopentadiene. *Indian J. Chem. Technol.* **1995**, *3*, 295−297.
(27) Parsinejad, F.; Arcari, C.; Metghalchi, H. Flame Structure and Burning Speed of JP-10 Air Mixtures. *Combust. Sci. Technol.* **2006**, *178*, 975−1000.
(28) Jiao, C. Q.; DeJoseph, C. A., Jr.; Garscadden, A. Dissociative ionization of JP-10 (C10H16) by electron impact. *Int. J. Mass spectrom.* **2007**, *266*, 92−96.
(29) Wang, S.; Gou, H.-j.; Fan, B.-c.; He, Y.-z.; Zhang, S.-t.; Cui, J.-p. Shock Tube Study of JP-10 Ignition Delay Time. *Chin. J. Chem. Phys.* **2007**, *20*, 48.
(30) Xing, Y.; Guo, Y.; Li, D.; Fang, W.; Lin, R. Measurement of Bubble-Point Vapor Pressure for Systems of Jp-10 with Ethanol. *Energy Fuels* **2007**, *21*, 1048−1051.
(31) Yang, F.; Guo, Y.; Xing, Y.; Li, D.; Fang, W.; Lin, R. Densities and Viscosities of Binary Mixtures of JP-10 with N-Octane or N-Decane at Several Temperatures. *J. Chem. Eng. Data* **2008**, *53*, 2237−2240.
(32) Su, X. H.; Hou, H. M.; Li, G.; Lin, R.; Cai, S.; Su, X.; Hou, H.; Li, G.; Lin, R.; Cai, S. Product Distribution of Thermal Cracking of Exo-Tetrahydrodicyclopentadiene. *Acta Chim. Sin.* **2009**, *67*, 587−592.
(33) Guo, F.; Cheng, X.; Zhang, H. Reaxff Molecular Dynamics Study of Initial Mechanism of JP-10 Combustion. *Combust. Sci. Technol.* **2012**, *184*, 1233−1243.
(34) Goh, K. H. H.; Geipel, P.; Hampp, F.; Lindstedt, R. P. Regime Transition from Premixed to Flameless Oxidation in Turbulent JP-10 Flames. *Proc. Combust. Inst.* **2013**, *34*, 3311−3318.
(35) Türker, L.; Variş, S.; Bayar, Ç. Ç. A Theoretical Study of JP-10 Hydroperoxidation. *Fuel* **2013**, *104*, 128−132.
(36) Qin, X.-M.; Xie, H.-J.; Yue, L.; Lu, X.-X.; Fang, W.-J. A Quantum Chemistry Study on Thermochemical Properties of High Energy-Density Endothermic Hydrocarbon Fuel JP-10. *J. Mol. Model.* **2014**, *20*, 2138.
(37) Gao, C. W.; Vandeputte, A. G.; Yee, N. W.; Green, W. H.; Bonomi, R. E.; Magoon, G. R.; Wong, H.-W.; Oluwole, O. O.; Lewis, D. K.; Vandewiele, N. M. JP-10 Combustion Studied with Shock Tube Experiments and Modeled with Automatic Reaction Mechanism Generation. *Combust. Flame* **2015**, *162*, 3115−3129.
(38) Seiser, R.; Niemann, U.; Seshadri, K. Experimental Study of Combustion of N-Decane and JP-10 in Non-Premixed Flows. *Proc. Combust. Inst.* **2011**, *33*, 1045−1052.
(39) Davidson, D.; Horning, D.; Herbon, J.; Hanson, R. Shock Tube Measurements of JP-10 Ignition. *Proc. Combust. Inst.* **2000**, *28*, 1687−1692.
(40) Li, S.; Varatharajan, B.; Williams, F. Chemistry of JP-10 Ignition. *AIAA J.* **2001**, *39*, 2351−2356.
(41) Mikolaitis, D. W.; Segal, C.; Chandy, A. Ignition Delay for Jet Propellant 10/Air and Jet Propellant 10/High-Energy Density Fuel/Air Mixtures. *J. Propul. Power* **2003**, *19*, 601−606.
(42) Zhao, L.; Yang, T.; Kaiser, R. I.; Troy, T. P.; Xu, B.; Ahmed, M.; Alarcon, J.; Belisario-Lara, D.; Mebel, A. M.; Zhang, Y. A Vacuum Ultraviolet Photoionization Study on High-Temperature Decomposition of JP-10 (Exo-Tetrahydrodicyclopentadiene). *Phys. Chem. Chem. Phys.* **2017**, *19*, 15780−15807.
(43) Johnson, S.; Davidson, D. F.; Hanson, R. K. Shock Tube/Laser Absorption Measurements of the Pyrolysis of JP-10 Fuel. *Combust. Flame* **2020**, *216*, 161−173.
(44) Sun, C.; Sung, C.; Wang, H.; Law, C. On the Structure of Nonsooting Counterflow Ethylene and Acetylene Diffusion Flames. *Combust. Flame* **1996**, *107*, 321−335.
(45) Allen, C.; Mittal, G.; Sung, C.-J.; Toulson, E.; Lee, T. An Aerosol Rapid Compression Machine for Studying Energetic-Nanoparticle-Enhanced Combustion of Liquid Fuels. *Proc. Combust. Inst.* **2011**, *33*, 3367−3374.
(46) Chase, M. W., Jr. Nist-Janaf Thermochemical Tables. *J. Phys. Chem. Ref. Data, Monogr.* **1998**, *9*.
(47) Liu, J. Z.; Chen, B. H.; Wu, T. T.; Yang, W. J.; Zhou, J. H. Ignition and Combustion Characteristics and Agglomerate Evolution Mechanism of Aluminum in Nal/JP-10 Nanofluid Fuel. *J. Therm. Anal. Calorim.* **2019**, *137*, 1369−1379.
(48) Xiu, T.-F.; Zhang, L.; Wang, F.; Zhang, X.; Zou, J.-J. Synthesis of Aluminum Nanoparticles as Additive to Enhance Ignition and Combustion of High Energy Density Fuels. *Front. Chem. Sci. Eng.* **2018**, *12*, 358−366.
(49) Chen, A.; Guan, X.; Li, X.; Zhang, B.; Zhang, B.; Song, J. Preparation and Characterization of Metalized JP-10 Gel Propellants with Excellent Thixotropic Performance. *Propellants, Explos., Pyrotech.* **2017**, *42*, 1007−1013.
(50) Chen, B. H.; Liu, J. Z.; Li, H. P.; Yang, W. J.; Cen, K. F. Laser Ignition and Combustion Characteristics of Al/JP-10 Nanofluid Droplet. *J. Therm. Anal. Calorim.* **2019**, *135*, 925−934.
(51) Chen, B. H.; Liu, J. Z.; Yao, F.; Li, H. P.; Zhou, J. H. Effect of Oleic Acid on the Stability and Rheology of Nanoaluminium/JP-10 Bi-Phase System. *Micro Nano Lett.* **2017**, *12*, 675−679.
(52) Epshteyn, A.; Yonke, B. L.; Miller, J. B.; Rivera-Díaz, J. L.; Purdy, A. P. Sonochemically Generated Air-Stable Bimetallic Nanopowders of Group 4 Transition Metals with Aluminum. *Chem. Mater.* **2013**, *25*, 818−824.
(53) Huba, Z. J.; Donakowski, M. D.; Epshteyn, A. Gram-Scale, Low Temperature, Sonochemical Synthesis of Stable Amorphous Ti−B Powders Containing Hydrogen. *Chem. Mater.* **2017**, *29*, 1467−1471.
(54) Epshteyn, A.; Weismiller, M. R.; Huba, Z. J.; Maling, E. L.; Chaimowitz, A. S. Optimization of a High-Energy Ti−Al−B Nanopowder Fuel. *Energy Fuels* **2017**, *31*, 1811−1819.
(55) Finn, M. T.; Chaloux, B. L.; Epshteyn, A. Exploring the Effects of Reaction Conditions on Morphology and Stability of Sonochemically Generated Ti−Al−B Fuel Powders. *Energy Fuels* **2020**, *34*, 11373−11380.
(56) Epshteyn, A.; Connell, T.; Huba, Z.; Fisher, B.; Yetter, R. *In Sonochemically Generated Amorphous Ti-Al-B Nanopowder: A High-Energy-Density Solid Fuel Additive*; American Chemical Society, 2017.
(57) Weismiller, M. R.; Huba, Z. J.; Tuttle, S. G.; Epshteyn, A.; Fisher, B. T. Combustion Characteristics of High Energy Ti−Al−B Nanopowders in a Decane Spray Flame. *Combust. Flame* **2017**, *176*, 361−369.
(58) Connell, T. L., Jr.; Yetter, R. A.; Risha, G. A.; Huba, Z. J.; Epshteyn, A.; Fisher, B. T. Enhancement of Solid Fuel Combustion in a Hybrid Rocket Motor Using Amorphous Ti−Al−B Nanopowder Additives. *J. Propul. Power* **2019**, *35*, 662−665.
(59) Fisher, B. T.; Cowart, J. S.; Weismiller, M. R.; Huba, Z. J.; Epshteyn, A. Effects of Amorphous Ti−Al−B Nanopowder Additives on Combustion in a Single-Cylinder Diesel Engine. *J. Eng. Gas Turbines Power* **2017**, *139*, 092802.
(60) Weismiller, M. R.; Huba, Z. J.; Epshteyn, A.; Fisher, B. T. Combustion of Sonochemically-Generated Ti−Al− B Nanopowders in a Premixed Methane/Air Dust Flame. *Combust. Flame* **2018**, *191*, 187−194.
(61) Weismiller, M. R.; Fisher, B. T.; Huba, Z. J.; Epshteyn, A.; Tuttle, S. G.; Williams, B. A. Combustion of Sonochemically-Generated

Amorphous Reactive Mixed-Metal Nanopowders in an N-Decane Spray Flame. *54th AIAA Aerospace Sciences Meeting*, 2016; pp 0686.
(62) Gan, Y.; Qiao, L. Combustion Characteristics of Fuel Droplets with Addition of Nano and Micron-Sized Aluminum Particles. *Combust. Flame* **2011**, *158*, 354−368.
(63) Sabourin, J. L.; Yetter, R. A.; Asay, B. W.; Lloyd, J. M.; Sanders, V. E.; Risha, G. A.; Son, S. F. Effect of Nano-Aluminum and Fumed Silica Particles on Deflagration and Detonation of Nitromethane. *Propellants, Explos., Pyrotech.* **2009**, *34*, 385−393.
(64) Smirnov, V. V.; Kostritsa, S. A.; Kobtsev, V. D.; Titova, N. S.; Starik, A. M. Experimental Study of Combustion of Composite Fuel Comprising N-Decane and Aluminum Nanoparticles. *Combust. Flame* **2015**, *162*, 3554−3561.
(65) Lucas, M.; Brotton, S. J.; Min, A.; Pantoya, M. L.; Kaiser, R. I. Oxidation of Levitated Exo-Tetrahydrodicyclopentadiene Droplets Doped with Aluminum Nanoparticles. *J. Phys. Chem. Lett.* **2019**, *10*, 5756−5763.
(66) Lucas, M.; Brotton, S. J.; Min, A.; Woodruff, C.; Pantoya, M. L.; Kaiser, R. I. Effects of Size and Prestressing of Aluminum Particles on the Oxidation of Levitated Exo-Tetrahydrodicyclopentadiene Droplets. *J. Phys. Chem. A* **2020**, *124*, 1489−1507.
(67) Brotton, S. J.; Malek, M. J.; Anderson, S. L.; Kaiser, R. I. Effects of Acetonitrile-Assisted Ball-Milled Aluminum Nanoparticles on the Ignition of Acoustically Levitated Exo-Tetrahydrodicyclopentadiene (JP-10) Droplets. *Chem. Phys. Lett.* **2020**, *754*, 137679.
(68) Perera, S. D.; Brotton, S. J.; Shinsato, H.; Kaiser, R. I.; Choi, Y.; Na, K. Catalytic Effects of Zeolite Socony Mobil-5 (ZSM-5) on the Oxidation of Acoustically Levitated Exo-Tetrahydrodicyclopentadiene (JP-10) Droplets. *J. Phys. Chem. A* **2021**, *125*, 4896−4909, DOI: 10.1021/acs.jpca.1c02892.
(69) Brotton, S. J.; Kaiser, R. I. Novel High-Temperature and Pressure-Compatible Ultrasonic Levitator Apparatus Coupled to Raman and Fourier Transform Infrared Spectrometers. *Rev. Sci. Instrum.* **2013**, *84*, 055114.
(70) Brotton, S. J.; Kaiser, R. I. In Situ Raman Spectroscopic Study of Gypsum ($CaSO_4 \cdot 2H_2O$) and Epsomite ($MgSO4 \cdot 7H_2O$) Dehydration Utilizing an Ultrasonic Levitator. *J. Phys. Chem. Lett.* **2013**, *4*, 669−673.
(71) Brotton, S. J.; Lucas, M.; Jensen, T. N.; Anderson, S. L.; Kaiser, R. I. Spectroscopic Study on the Intermediates and Reaction Rates in the Oxidation of Levitated Droplets of Energetic Ionic Liquids by Nitrogen Dioxide. *J. Phys. Chem. A* **2018**, *122*, 7351−7377.
(72) Hutsebaut, D.; Vandenabeele, P.; Moens, L. Evaluation of an Accurate Calibration and Spectral Standardization Procedure for Raman Spectroscopy. *Analyst* **2005**, *130*, 1204−1214.
(73) Morozov, A. N.; Mebel, A. M.; Kaiser, R. I. A Theoretical Study of Pyrolysis of Exo-Tetrahydrodicyclopentadiene and Its Primary and Secondary Unimolecular Decomposition Products. *J. Phys. Chem. A* **2018**, *122*, 4920−4934.
(74) Frisch, M.; Trucks, G.; Schlegel, H. B.; Scuseria, G. E.; Robb, M. A.; Cheeseman, J. R.; Scalmani, G.; Barone, V.; Mennucci, B.; Petersson, G. *Gaussian 09*, Revision D. 01, Gaussian, 2009.
(75) Møller, C.; Plesset, M. S. Note on an Approximation Treatment for Many-Electron Systems. *Phys. Rev.* **1934**, *46*, 618−622.
(76) Krishnan, R.; Binkley, J. S.; Seeger, R.; Pople, J. A. Self-Consistent Molecular Orbital Methods. XX. A Basis Set for Correlated Wave Functions. *J. Chem. Phys.* **1980**, *72*, 650−654.
(77) Francl, M. M.; Pietro, W. J.; Hehre, W. J.; Binkley, J. S.; Gordon, M. S.; DeFrees, D. J.; Pople, J. A. Self-Consistent Molecular Orbital Methods. XXIII. A Polarization-Type Basis Set for Second-Row Elements. *J. Chem. Phys.* **1982**, *77*, 3654−3665.
(78) McLean, A. D.; Chandler, G. S. Contracted Gaussian Basis Sets for Molecular Calculations. I. Second Row Atoms, Z=11−18. *J. Chem. Phys.* **1980**, *72*, 5639−5648.
(79) Weigend, F.; Ahlrichs, R. Balanced Basis Sets of Split Valence, Triple Zeta Valence and Quadruple Zeta Valence Quality for H to Rn: Design and Assessment of Accuracy. *Phys. Chem. Chem. Phys.* **2005**, *7*, 3297−3305.
(80) Lee, C.; Yang, W.; Parr, R. G. Development of the Colle-Salvetti Correlation-Energy Formula into a Functional of the Electron Density. *Phys. Rev. B* **1988**, *37*, 785.
(81) Beck, A. D. Density-Functional Thermochemistry. III. The Role of Exact Exchange. *J. Chem. Phys.* **1993**, *98*, 5648−5656.
(82) Stephens, P. J.; Devlin, F. J.; Chabalowski, C. F.; Frisch, M. J. Ab Initio Calculation of Vibrational Absorption and Circular Dichroism Spectra Using Density Functional Force Fields. *J. Phys. Chem.* **1994**, *98*, 11623−11627.
(83) Grimme, S.; Antony, J.; Ehrlich, S.; Krieg, H. A Consistent and Accurate Ab Initio Parametrization of Density Functional Dispersion Correction (DFT-D) for the 94 Elements H-Pu. *J. Chem. Phys.* **2010**, *132*, 154104.
(84) Palenik, M. C. Initial Estimate for Minimum Energy Pathways and Transition States Using Velocities in Internal Coordinates. *Chem. Phys.* **2021**, *542*, 111046.
(85) Simons, J.; Joergensen, P.; Taylor, H.; Ozment, J. Walking on Potential Energy Surfaces. *J. Phys. Chem.* **1983**, *87*, 2745−2753.
(86) Peng, C.; Bernhard Schlegel, H. Combining Synchronous Transit and Quasi-Newton Methods to Find Transition States. *Isr. J. Chem.* **1993**, *33*, 449−454.
(87) Ayala, P. Y.; Schlegel, H. B. A Combined Method for Determining Reaction Paths, Minima, and Transition State Geometries. *J. Chem. Phys.* **1997**, *107*, 375−384.
(88) Perdew, J. P.; Burke, K.; Ernzerhof, M. Generalized Gradient Approximation Made Simple. *Phys. Rev. Lett.* **1996**, *77*, 3865−3868.
(89) Perdew, J. P.; Burke, K.; Ernzerhof, M. Generalized Gradient Approximation Made Simple [Phys. Rev. Lett. 77. *Phys. Rev. Lett.* **1996**, *77*, 3865−3868.
(90) Becke, A. D. Density Functional Thermochemistry. I. The Effect of the Exchange-Only Gradient Correction. *J. Chem. Phys.* **1992**, *96*, 2155−2160.
(91) Becke, A. D. Density Functional Thermochemistry. II. The Effect of the Perdew−Wang Generalized-Gradient Correlation Correction. *J. Chem. Phys.* **1992**, *97*, 9173−9177.
(92) Purvis, G. D. P., III; Bartlett, R. J. A Full Coupled-Cluster Singles and Doubles Model: The Inclusion of Disconnected Triples. *J. Chem. Phys.* **1982**, *76*, 1910−1918.
(93) Hampel, C.; Peterson, K. A.; Werner, H.-J. A Comparison of the Efficiency and Accuracy of the Quadratic Configuration Interaction (QCISD), Coupled Cluster (CCSD), and Brueckner Coupled Cluster (BCCD) Methods. *Chem. Phys. Lett.* **1992**, *190*, 1−12.
(94) Knowles, P. J.; Hampel, C.; Werner, H. J. Coupled Cluster Theory for High Spin, Open Shell Reference Wave Functions. *J. Chem. Phys.* **1993**, *99*, 5219−5227.
(95) Deegan, M. J. O.; Knowles, P. J. Perturbative Corrections to Account for Triple Excitations in Closed and Open Shell Coupled Cluster Theories. *Chem. Phys. Lett.* **1994**, *227*, 321−326.
(96) Frisch, M. J.; Trucks, G. W.; Schlegel, H. B.; Scuseria, G. E.; Robb, M. A.; Cheeseman, J. R.; Scalmani, G.; Barone, V.; Petersson, G. A.; Nakatsuji, H.; Petrone; et al. *Gaussian 16*. Revision. C.01: Wallingford, CT, 2016.
(97) Lee, Y. K.; Manceron, L.; Pápai, I. An IR Matrix Isolation and DFT Theoretical Study of the First Steps of the Ti(0) Ethylene Reaction: Vinyl Titanium Hydride and Titanacyclopropene. *J. Phys. Chem. A* **1997**, *101*, 9650−9659.
(98) Andrews, L.; Cho, H.-G.; Wang, X. Reactions of Methane with Titanium Atoms:CH3T$_i$H ,CH2T$_i$H2 ,Agostic Bonding ,and (CH3)-2$_T$iH2. *Inorg. Chem.* **2005**, *44*, 4834−4842.
(99) Burkholder, T. R.; Andrews, L. Matrix Infrared Spectra of Aluminum, Gallium, and Indium Complexes with Acetylene. *Inorg. Chem.* **1993**, *32*, 2491−2496.
(100) Chertihin, G. V.; Andrews, L.; Taylor, P. R. Reactions of Pulsed-Laser-Evaporated Al with C and C_2H_2. Infrared Spectra and Casscf Calculations for AlC, Al_2C, Al_2C_2, and AlC_2H. *J. Am. Chem. Soc.* **1994**, *116*, 3513−3518.
(101) Jacox, M. E. Vibrational and Electronic Energy Levels of Polyatomic Transient Molecules. Supplement A. *J. Phys. Chem. Ref. Data* **1998**, *27*, 115−393.

(102) Andrews, L.; Lanzisera, D. V.; Hassanzadeh, P.; Hannachi, Y. Reactions of Laser-Ablated Boron Atoms with Ethylene and Ethane. Infrared Spectra and Dft Calculations for Several Novel BC_2HX (X = 1, 2, 3, 4, 5) Molecules. *J. Phys. Chem. A* **1998**, *102*, 3259−3267.
(103) Andrews, L.; Hassanzadeh, P.; Martin, J. M. L.; Taylor, P. R. Pulsed Laser Evaporated Boron Atom Reactions with Acetylene. Infrared Spectra and Quantum Chemical Structure and Frequency Calculations for Several Novel Organoborane BC_2H_2 and HBC_2 Molecules. *J. Phys. Chem.* **1993**, *97*, 5839−5847.
(104) Jacox, M. E. Vibrational and Electronic Energy Levels of Polyatomic Transient Molecules. Supplement B. *J. Phys. Chem. Ref. Data* **2003**, *32*, 1−441.
(105) Manceron, L.; Andrews, L. Infrared Spectrum of the Aluminum Monoethylene Molecule in Solid Argon. *J. Phys. Chem.* **1989**, *93*, 2964−2970.
(106) Socrates, G. *Infrared and Raman Characteristic Group Frequencies: Tables and Charts*, 3rd ed.; John Wiley & Sons: New York, 2004.
(107) Buixaderas, E.; Anghel, E. M.; Atkinson, I.; Simon, P.; Bratan, V.; Petrescu, S. Combustion Synthesis and Structural Characterization of the TiB_2−($Na_2O{\cdot}2B_2O_3$−Al_2O_3) Composites. *Ceram. Int.* **2015**, *41*, 2680−2689.
(108) Buixaderas, E.; Maria Anghel, E.; Petrescu, S.; Osiceanu, P. Structural Investigation in the TiB_2−($Na_2O{\cdot}B_2O_3{\cdot}Al_2O_3$) System. *J. Solid State Chem.* **2010**, *183*, 2227−2235.
(109) Abu Suilik, S. B.; Ohshima, M.; Tetsui, T.; Hasezaki, K. Selected Interlayer of Diamond Deposition on Γ-Tial Intermetallic Compounds Prepared by Microwave-Plasma Assisted Cvd. *Materials Science Forum*; Trans Tech Publications, 2010; pp 425−430.
(110) Loa, I.; Kunc, K.; Syassen, K.; Bouvier, P. Crystal Structure and Lattice Dynamics of AlB_2 under Pressure and Implications for MgB_2. *Phys. Rev. B* **2002**, *66*, 134101.
(111) Loa, I.; Kunc, K.; Syassen, K. MgB_2 and AlB_2 at High Pressures. *High Pressure Res.* **2003**, *23*, 129−134.
(112) Banu, A.; Anghel, E. M.; Marcu, M.; Georgescu, L. *The Oxidation Behavior of Titanium Aluminde at 850°C Energy*; Environment and Material Science, 2012.
(113) Huong, P. V. Diamond and Diamond Simulants as Studied by Micro-Raman Spectroscopy. *Mater. Sci. Eng., B* **1992**, *11*, 235−242.
(114) Kochuev, D. A.; Khorkov, K. S.; Abramov, D. V.; Arakelian, S. M.; Prokoshev, V. G. Titanium-Carbide Formation in a Liquid Hydrocarbon Medium by Femtosecond Laser Irradiation. *J. Surf. Invest.* **2018**, *12*, 1220−1223.
(115) Chaliyawala, H. A.; Srinivas, G.; Bera, P.; Siju; Kumar, P.; Khan, J.; Barshilia, H. C. Improved Thermal Stability, Mechanical and Tribological Properties of Reactively Sputtered Si Doped Tialc Nanostructured Hard Coatings. *Surf. Coat. Technol.* **2016**, *288*, 95−104.
(116) Kunka, C.; Awasthi, A.; Subhash, G. Evaluating Boron-Carbide Constituents with Simulated Raman Spectra. *Scr. Mater.* **2017**, *138*, 32−34.
(117) Lopez-Quintas, I.; Oujja, M.; Sanz, M.; Benitez-Cañete, A.; Chater, R. J.; Cañamares, M. V.; Marco, J. F.; Castillejo, M. Micrometric Rods Grown by Nanosecond Pulsed Laser Deposition of Boron Carbide. *Appl. Surf. Sci.* **2015**, *328*, 170−176.
(118) Linstrom, P. J. M.; Mallard, W. G. NIST Chemistry Webbook, Nist Standard Reference Database Number 69. https://doi.org/10.18434/T4D303 (accessed 9 November 2020).
(119) Gaydon, A. *The Spectroscopy of Flames*. 2d ed.; Chapman and Hall: London, New York, 1974.
(120) Huber, K. P.; Herzberg, G. Constants of Diatomic Molecules. In *Molecular Spectra and Molecular Structure: IV. Constants of Diatomic Molecules*; Huber, K. P., Herzberg, G., Eds.; Springer US: Boston, MA, 1979, pp 8−689. DOI: 10.1007/978-1-4757-0961-2_2
(121) Phillips, J. G. The Gamma'-System of the TiO Molecule. *Astrophys. J.* **1969**, *157*, 449.
(122) Żyrnicki, W.; Palmer, H. B. Band Spectra of the Γ′ System of the TiO Molecule. *Physica B+C* **1976**, *84*, 152−154.
(123) Lowater, F. The Band Systems of Titanium Oxide. *Proc. Phys. Soc.* **1928**, *41*, 557−568.
(124) McKemmish, L. K.; Masseron, T.; Sheppard, S.; Sandeman, E.; Schofield, Z.; Furtenbacher, T.; Császár, A. G.; Tennyson, J.; Sousa-Silva, C. Marvel Analysis of the Measured High-Resolution Rovibronic Spectra of $^{48}Ti^{16}O$. *Astrophys. J., Suppl. Ser.* **2017**, *228*, 15.
(125) Maksyutenko, P.; Parker, D. S. N.; Zhang, F.; Kaiser, R. I. An LIF Characterization of Supersonic BO ($X^2\Sigma^+$) and CN ($X^2\Sigma^+$) Radical Sources for Crossed Beam Studies. *Rev. Sci. Instrum.* **2011**, *82*, 083107.
(126) Saba, M.; Kato, T.; Oguchi, T. Reaction Modeling Study on the Combustion of Aluminum in Gas Phase: The Al + O_2 and Related Reactions. *Combust. Flame* **2021**, *225*, 535−550.